MIKE LAUGE

dE/dx MEASUREMENTS IN THE ATLAS DETECTOR

MSC THESIS
NIELS BOHR INSTITUTE, UNIVERSITY OF COPENHAGEN

dE/dx MEASUREMENTS IN THE ATLAS DETECTOR

MIKE LAUGE

NIELS BOHR INSTITUTE,
UNIVERSITY OF COPENHAGEN

Supervisor Dr. T. Petersen

dE/dx Measurements in the ATLAS Detector
MSc Thesis, University of Copenhagen
viii + 59 pages; illustrated, with bibliographic references

Set in 10/14 pt Palatino Linotype using pdfLaTeX with the Tufte-LaTeX package
Cover art: University of Copenhagen logo grid

Thesis submitted on 6 April 2017
for the completion of the degree of Master of Science (MSc) in Physics
at the Niels Bohr Institute, University of Copenhagen.

First printing, April 2017

Contents

Abstract

The ATLAS Pixel detector is able to provide a measurement of the specific energy loss dE/dx for tracks from proton-proton collisions at high center of mass. This thesis will present a study of the this measurement and evaluate if cuts stated in earlier studies (2011) are still needed, or if the upgrades made to the Pixel Detector have resulted in needed adjustments to the cuts. The study introduce a new method of calculating the dE/dx of a track. This is done by using the knowledge of the distribution of dE/dx to likelihood fit the hits of the individual track.

In additions to this a study of the dependency of dE/dx on β is completed, showing that the dependency fulfill as simplification of the Bethe-Bloch formula.

The thesis finishes with a study on the uncertainty of β, which indicates a correlation between increasing uncertainty as the value of dE/dx increases.

The studies uses data recorded in the $\sqrt{s} = 13$TeV proton-proton collisions during the 2016 run period and Monte Carlo simulation samples with corresponding conditions.

Disclaimer

The results presented in this thesis, be they plots or figures, are based on official ATLAS data from the mc15 simulation project and Run 2. These are the product of the author's own work and have *not* been approved by the ATLAS Collaboration. Any replication of these results should clearly reflect this fact.

Acknowledgement

First and foremost I owe my supervisor Troels Petersen a big thank for being a true inspiration, always willing to help whenever I found myself stuck and unable to solve a problem by myself. Also I am so grateful for his what seemed unlimited understanding after I suffered a concussion halfway through my thesis period, A concussion that made me unable to preform the way I wanted to, but nevertheless Troels made sure to have the data, that I had struggled to get ready for analysis, ready for my return, which saved me many hours of work producing my data samples.

Another great thanks goes to Daniel Nielsen for being an excellent programmer always willing to spend time solving new interesting 'Segmentation Violations' which a seem to have an explicit talent to produce. But also for bringing an warm and welcoming atmosphere to the office together with Freja Thoresen, it made the never ending bug fixing and ROOT plotting somewhat easier.

Introduction

The aim of this thesis was to look into the energy loss (dE/dx) measurements made in the ATLAS Pixel Detector and how to improve these.

Early in the process it turned out that there where no data samples available and then the process of getting data that was ready for analysis, turned into a bigger and more time consuming task than we expected. As mentioned above my first and main task was to look into the dE/dx measurement and try to improve on the already exciting procedure. Unfortunately it turned out that the person who made this analysis have a policy the he do not share his scripts. This of course made it hard to directly improve on the current method and forced me to change my approach. As a result I used a previous dE/dx analysis made in 2010 [1] and used this as a cookbook. So where I normally would have gotten a working script and then been able to change a few things here are there and then look at how it would change the result, I had to produce all the script and analysis myself. This gave me a much deeper understanding of the process from measurement to result, e.g. what defines a good hit and which tracks should be excluded. Nevertheless if my analysis is not exactly the same as the one I'm trying to improve it is hard to do any kind of comparison.

During the thesis process it became clear that improving the measurement of dE/dx was possible, but only by the sacrifices of increased processing-time. With this result a new aim was needed and this was provided by Troels C. Petersen who had received a plot showing the dE/dx's dependency on β. This gave the opportunity to test this dependency and as a more interesting result the data necessary gave an estimate of the uncertainty of the β measurement.

The thesis starts with a brief introduction to the theory of particle physics and the Standard Model in Section 1.1, then summing up particle detection in Section 1.2.

In Section 2.1 The LHC Experiment as a hole is introduced and throughout this Chapter the experiment is explained narrowing in on the part with importance of this thesis, giving an overview of The ATLAS detector in Section 2.2, the silicon detectors of the Inner Detector in Section 2.3 and general track reconstruction in Section 2.5.

Chapter 3 is the analysis and contains two parts, first Section 3.1 and 3.2 goes through the data used in the analysis and how some data is excluded. Section 3.3 is the analyses of the dE/dx measurement while Section 3.4 looks into dE/dx's dependency on β and the uncertainty estimate of β.

I Theory

1.1 Particle Physics

The main purposes of this thesis is to refine a technique that is already in use in the search for new particles. To accomplish this a sufficient understanding of currently accepted theories in particle physics and their predictions is required. Therefore this sections will give a brief overview of the Standard Model (SM) of particle physics, introducing the theory, its associated particles and their interactions. It is not the intention to present a complete account of the Standard Model, but rather to explain the essentials needed later on.

1.1.1 The Standard Model

In the search of the smallest building blocks of the universe, those which are considered to have no constituents and no internal structure are called the elementary particles. The Standard Model (SM) was developed throughout the later half of the 20th century and is the current theory that explains particle physics to the greatest extend. In the SM both forces and matter are represented as particles. The matter particles are all fermions and are either quarks or leptons all with half-integer spin. Fermions respect the Pauli exclusion principle and each fermion has a corresponding antiparticle. Both quarks and leptons is divided into three generations, for each generation the particles gets progressively more massive.

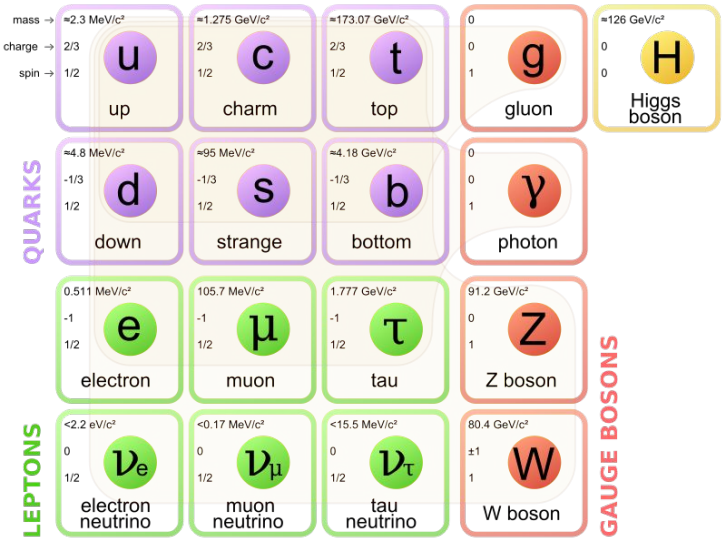

Figure 1.1: The elementary particles of the Standard Model [2]

The force carrying particles also known as Gauge Bosons (marked with a red square in Figure 1.1) is associated with all interactions of the SM.

The gluon [g], is the force carrier of the the strong interaction known from Quantum Chromodynamics (QCD), it interacts with all color charged particles. Since the gluon is color charged, they can also interact among themselves.

The photon [γ], is the force carrier of the electromagnetic interaction as part of electroweak interaction, it interacts with all electrically charged particles. Since it is not electrically charged, photons does not self-interact.

The force carriers of the weak interaction is the $W^{\pm}$ and Z bosons, they interact with particles of different flavors. They interact with themselves and each other.

The quarks (in the purple boxes of Figure 1.1) generations is 1. the up (u), 2. the charme (c) and 3. the top (t) all carrying the charge $+2/3$ and referred to as up-type. Their corresponding flavor doublets is respectively down (d), strange (s) and bottom (b), all with the charge $-1/3$ and referred to as down-type. Furthermore all quarks carries weak isospin, therefore all quarks interacts with all force carriers in the SM.

The leptons (in the green boxes of Figure 1.1) generations is 1. the electron [e^-], 2. the muon [μ] and 3. the tau [τ] all carrying the charge -1 and all with their corresponding neutral flavor doublets respectively ν^e, ν^μ and ν^τ. All leptons carries weak isospin and therefore interacts with the weak force, as mentioned above the electron, muon and tau all carries charge and therefore also interacts through electromagnetic interaction. A summary of which bosons interacts with the different SM particles is shown in Figure 1.2.

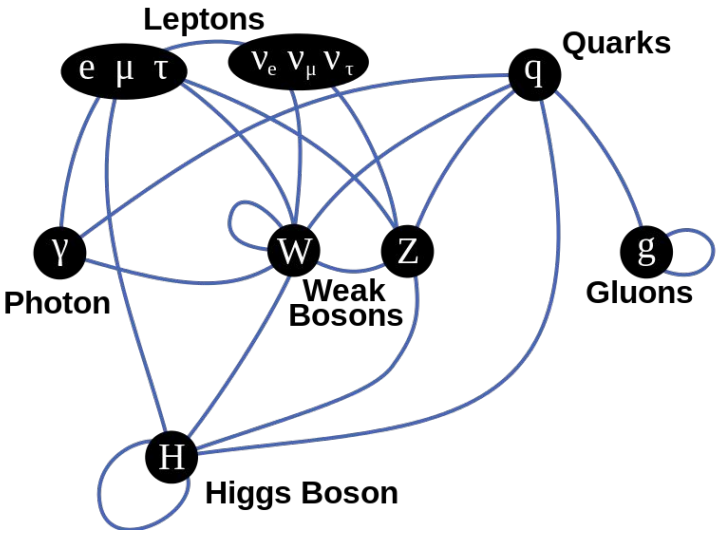

Figure 1.2: An interaction diagram of the elementary particles of the Standard Model [2]

1.2 Principles of Particle Detection

To study the particles of the SM a machine to detect them is needed, the following sections aims to give a overview of how this is done in The Atlas Experiment. The Silicon pixel detectors [3][4] are chosen for high-resolution particle tracking detectors in high energy physics. Despite their small material budget they ensure a fast readout and are mechanically stable, which is required for good vertex resolution.

1.2.1 Particles Interacting with Matter

The properties of a particle such as charge, mass and energy determines how it will behave when passing though matter. How these properties influent on its behavior is discussed in the following.

1.2.1.1 Charged Particles in Matter

Particles with a mass well above the mass of an electron ($M >> m_e$) and sufficient kinetic energy that enters a material, will lose energy predominantly due to ionization and excitation. These processes lead to the release of free charge carriers which can be extracted by an externally applied electrical field. It is therefore the most widely used mechanism to detect relativistic charged particle. The process was first discovered and described in quantum mechanics by Bethe and Bloch[5]. The average energy loss per distance traveled in a material is given by the Bethe-Bloch formula [5]

$$-\left\langle \frac{dE}{dx} \right\rangle = 2\pi N_A r_e^2 m_e c^2 \frac{Z}{A}\frac{z^2}{\beta^2}\left\{ ln\left(\frac{2m_e c^2\beta^2\gamma^2 W_{\max}}{I^2}\right) - 2\beta^2 - \delta - 2\frac{C}{Z}\right\} \tag{1.1}$$

Where N_A Avogadro's number, r_e is the electron radius, m_e the electron mass, Z the atomic number of the absorbing material, A atomic weight of absorbing material, z the charge of an incident particle in units of e, δ the density correction, C the shell correction and $W_{\max}$ the maximum energy transfer in a single collision. A usual conversion is that the average energy loss is normalized to the density ρ of the material without explicit notification.

The dependency of $\langle \frac{dE}{dx} \rangle$ on $\beta\gamma$ [6] is shown in Figure 1.3. In the case of $\beta\gamma < 0.1$ other processes than ionization dominates the energy loss, eq. 1.1 is not yet valid. Above these values, the $1/\beta^2$-term dominates the behavior at first, reaching a minimum at $\beta\gamma \approx 4$ followed by a rise proportional to $\ln\beta\gamma$. This behavior can be understood by a semi-classical approach [7], the $1/\beta^2$-behavior has it origin in the kinematics of the individual energy transfer, while the $\ln\beta\gamma$-behavior comes from Coulomb potential when integrating over the kinematically allowed range of impact parameters. At higher $\beta\gamma$ the logarithmic rise is reduced by polarization effects in the material. This reduction in $\langle dE/dx \rangle$ is described by $\delta(\beta\gamma)$, it is material dependent since the polarizations effect is strongly influenced by the density and chemical structure of a given material.

For highly relativistic particles the logarithmic rise after the minimum leaves $\langle dE/dx \rangle$ close to the minimum: it rises to a value between 10% and several 10% of the minimum value, depending on the material. Therefore, the minimal value $\langle dE/dx \rangle_{\min}$ is typical for a large range of $\beta\gamma$. It can be considered a worst case scenario for detectors since the signal that can be detected is smallest. This leads to the definition of a minimum ionizing particle (m.i.p), that is often used to quantify detector response without need to refer to a specific particle. For this hypothetical particle it is a good approximation to use $\langle dE/dx \rangle_{\min} \approx 1.5\text{MeVcm}^2/\text{g}$, nearly independent of the material that the particle traverses [4].

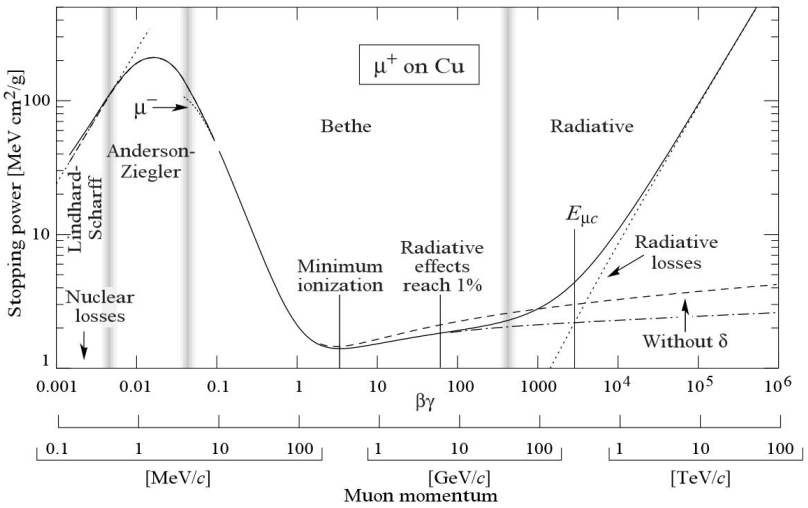

Figure 1.3: Energy loss of μ in copper, illustrating the functional behavior of energy loss of ionising particles in matter. [6]

The individual values of dE/dx in a detector is distributed around the $\langle dE/dx \rangle$ discussed above. Most of these individual scattering processes has little or a modest amount of energy transferred compared to the maximum possible kinetic energy transfer ($T_{\max}$), since energy transfers close to $T_{\max}$ only happens rarely. A small part of the interactions between the ionizing particle and the material, leads to a highly asymmetric distribution of the deposited energy ΔE, which only gets symmetric again after a large number of interactions obtained by either a thick or dense material. This transition can be defined by [4]

$$\kappa = \frac{\xi}{T_{\max}} \tag{1.2}$$

where ξ is given by

$$\xi = \frac{K}{2} z^2 \frac{Z}{A} \frac{1}{\beta^2} \rho d \tag{1.3}$$

Where all symbols are defined as in eq. 1.1 and d is the thickness of the material. In the case of a thin absorber ($\kappa \to 0$) can be described by a Landau-distribution [8].

$$L(\lambda) = \frac{1}{\pi} \int_0^\infty \exp(-u \ln u - u\lambda) \sin \pi u du \tag{1.4}$$

Where λ is given by

$$\lambda = \frac{\Delta E - (\Delta E)_{\text{m.p.v.}}}{\xi} \tag{1.5}$$

Where $(\Delta E)_{\text{m.p.v.}}$ is

$$(\Delta E)_{\text{m.p.v.}} = \xi \left[\ln \frac{2 m_e c^2 \beta^2 \gamma^2}{I} + \ln \frac{\xi}{I} + 0.2 - \beta^2 - \delta(\beta\gamma) \right] \tag{1.6}$$

And denotes the most probable value [9]. In Figure 1.4 a Landau function for a m.i.p transversing silicon with three different thicknesses d, is shown. The most probable value $(\Delta E)_{\text{m.p.v.}}/d$ changes as d change, while the average $\langle \Delta E \rangle / d = \langle dE/dx \rangle$ stays the same. The full width half maximum (FWHM) is approximately 4ξ, independent of the changed parameters.

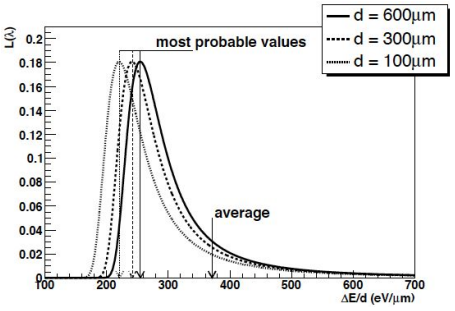

Figure 1.4: The distribution of ΔE of a m.i.p. in silicon with the thickness d normalized to d by a Landau function defined i eq. 1.4.[4]

1.2.1.2 Electrons and Photons in Matter

As described earlier the Bethe-Bloch formula assumes that the particle passing through matter is heavier than the shell electron it interacts with. Therefore due to the equal mass of the interacting particles as well as the fact that the incident electron and the shell electron are quantum mechanically indistinguishable, a modification is necessary for electrons. Also a contribution from Bremsstrahlung needs to be considered. Bremsstrahlung is emitted if an electron is scattered in the field of a nucleus, due to the acceleration of the electron. It represents the largest part of energy loss for electrons at high energies. The energy loss is proportional to the energy E of the incident particle [10], given by

$$-\left\langle \frac{dE}{dx} \right\rangle_{\text{rad}} = \frac{E}{X_0} \tag{1.7}$$

The constant of proportionality depends only on the material and is called the radiation length X_0, it is an expression for the mean distance over which a high energetic electron loses $1/e$ of its energy via Bremsstrahlung alone.The mean free path due to pair creation λ is proportional to X_0. It is necessary to minimize X_0 in tracking detectors to decrease the possibility of pair creation.

The Bethe-Bloch formula 1.1 express the average energy loss in a material of the thickness dx. When analyzing energy loss of particles in matter a statistical approach is needed. For particles passing trough thick layers the energy loss for each particle is described by a Gaussian distribution, with a mean given by the Bethe-Bloch equation. As the layer get thinner the distribution will change, when the layer thickness is thinner then $100\mu m$ the energy loss is better described by a Landau distribution as it is shown in Figure 1.5 [11]. The change in the distribution originate from the fact, that as the layer gets thinner the number of collisions for each particle will decrease. The Landau distribution is known for its long tail, in this case towards high energy loss and is mainly caused by particles having direct collisions with electrons. Since the high-energy tail moves the mean towards higher energy loss the mean energy loss value is higher than the most probable value.

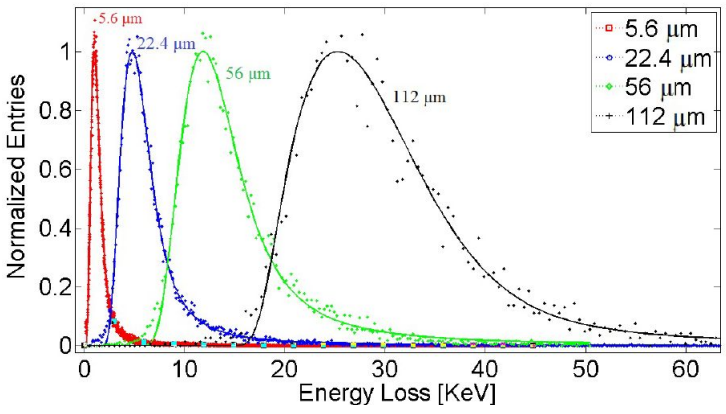

Figure 1.5: Energy loss distributions with fits for $12GeV$ protons passing though several silicon thicknesses. [11]

1.2.1.3 Photons in Matter

Since photons has no charge, there is no inelastic collisions with electrons, resulting in a different behavior than the one described in the earlier section, when interacting with matter.

The most important processes are the photoelectric effects, Compton scattering and pair production. At lower energy (below $100 - 300$keV) photons interact mostly via the photoelectric effect, which means that an electron is emitted by absorbing a photon, but only if the energy of the photon is larger than the binding energy of the electron. The kinetic energy of the electron will be equal to initial energy of the photon subtracted by the binding energy of the electron. As the frequency of the photoelectric effect decreases the Compton effect starts dominating until the photon's energy reaches 10MeV. An electron absorbs energy from the photon and is excited while the photon continues in a new direction with the remaining energy. Neither the electron nor the photon provides information about the initial photon. At high energies pair production is the most important process, if the photon energy is twice the electron mass or higher, an electron positron pair is produced hence the photon is absorbed and does not enter the calorimeter system, it is only possible to reconstruct by a challenging process, from the electron positron pair. The cross-section of these processes depends on the energy of the photon and the material, as shown in Figure 1.6.

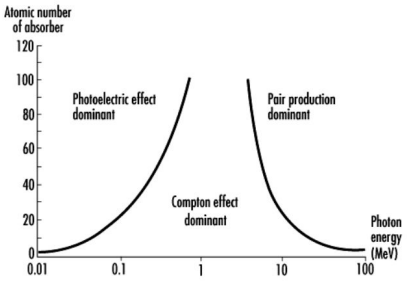

Figure 1.6: Above is shown the regions in which each type of photon interaction dominates as a function of photon energy and atomic number of absorber. [12]

Both in the case of photoelectric effect and pair production the electron is eventually absorbed and photons are re-emitted and as a result the beam of photons is attenuated passing through matter. The loss of intensity is exponential and can be expressed by the thickness of the material that the beam is passing through

$$I(x) = I_0 e^{-\mu x} \tag{1.8}$$

I_0 is the initial intensity, x is the thickness of the material and μ is the material-specific and energy-dependent mass attenuation coefficient. As described earlier, in the case of Compton scattering the photon is not absorbed, but the energy of the photon is changed.

In detectors used for high-energy physics pair production is the dominating factor, in tracking and vertexing detectors it is an unwanted process: to do measurement of a photon using the tracks of the electron positron pair is complicated, and the measurements of the photons properties in subsequent detectors is no longer possible since the photon never arrives at these detectors. The mean free path due to pair production is $\lambda = \frac{9}{7} X_0$ [4]. Therefore a X_0 as small as possible is essential to keep the probability of pair production low.

1.2.1.4 Multiple Scattering

In addition to the processes described above, charged particles will typically scatter elastically off the nuclei in the material [4]. This type of scattering is described by the Rutherford formula[4], showing that the cross-section is large for small scattering angles. The total

scattering in a material of the thickness d is therefore the result of a large number of small contributions independent of each other, this phenomena is called multiple scattering. The distribution of the total scattering angle θ can be approximated by a Gaussian distribution, the mean at zero and the standard deviation given by eq. 1.9 [13].

$$\sigma_\theta \approx \frac{13.6\text{MeV}}{pv}\sqrt{\frac{d}{X_0}} \tag{1.9}$$

where p is the momentum and v the velocity of the incident particle. For low momentum particles this greatly decreases the precision by which the direction of the particle can be measured, due to the inverse proportionality of σ_θ to p.

II The Experiment

2.1 The Large Hadron Collider

The Large Hadron Collider (LHC) [14] is a two-ring-superconducting-hadron accelerator and collider. It is a proton-proton collider with a design centre-of-mass energy of $14TeV$. Furthermore, the LHC can collide heavy ions. The construction of LHC was approved by the council of The European Organization for Nuclear Research (or CERN from the acronym for the French Conseil EuropÃl'en pour la Recherche NuclÃl'aire) in December 1994. LHC was installed in the circular tunnel located at CERN at the border between France and Switzerland, originally (until 2000) used by the Large Electron-Positron Collider (LEP).

Radio frequency superconducting cavities accelerate protons with an accelerating gradient of $16MV/m$. The protons is grouped in bunches, the number of protons in each bunch is around $N_p = 1.15 \cdot 10^{11}$ and the number of bunches in the ring at high luminosity is $n_b = 2808$. The bunches are separated by $25ns$, which corresponds to a collision rate of $f = 40MHz$. Superconducting magnets with a magnetic field of about $8.4T$ is used, to bend and focus the beam of particles around the ring. The particles are separated in two beam pipes with opposite directions before they collide at one of the four detectors in LHC.

The main parameter of LHC is the luminosity [L] which are given by

$$L = \frac{N_p \cdot f \cdot n_b}{4\pi \cdot \sigma_x \cdot \sigma_y} \tag{2.1}$$

Where N_p and n_b, as mentioned earlier, is the number of protons per bunch and the number of bunches per beam respectively. f is the revolution frequency and $\sigma_x \cdot \sigma_y$ is the beam dimensions at the interaction point. In general the number of event dN per time dt also known as the event rate is given by

$$\frac{dN}{dt} = L \times \sigma \tag{2.2}$$

The event rate depends on the luminosity L and the cross-section σ, due to the nature of proton-proton collision the cross-section of rare processes are many orders of magnitudes smaller than e.g. the jet production cross-section. To observe rare events the luminosity must be high, for instance the cross-section of the Higgs boson is much smaller than the cross-section of the W or Z boson. In Figure 2.1 an overview of the production cross-section for SM particles is shown.

The total number of particles created in an accelerator is proportional to the integrated luminosity.

$$\mathfrak{L} = \int L(t)dt \tag{2.3}$$

With the unit cm^{-2} normally expressed in inverse femtobarn [fb^{-1}].

In 2009 the first collisions took place at a center-of-mass energy of $900GeV$, in 2010 and 2011 the energy was increased to $7TeV$ and

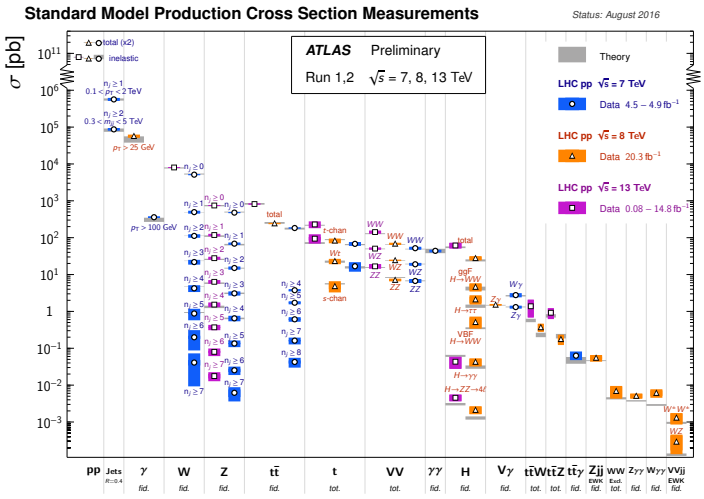

Figure 2.1: Summary of several Standard Model total and fiducial production cross section measurements, corrected for leptonic branching fractions, compared to the corresponding theoretical expectations. Not all measurements are statistically significant yet.From https://atlas.web.cern.ch/Atlas/GROUPS/PHYSICS/CombinedSummaryPlots/SM/index.html#ATLAS_b_SMSummary_FiducialXsect

in 2012 the energy reached 8*TeV*. Early 2013 Run 1 was shut down and LHC had a major 2-year long upgrade to enable collisions at 14*TeV*. In June 2015 LHC started delivering data from 13*TeV* collisions after almost 2 years offline. The total integrated luminosity that was delivered by LHC and the amount recorded by ATLAS in the years 2011, 2012, 2015 and 2016 is shown in Figure 2.2.

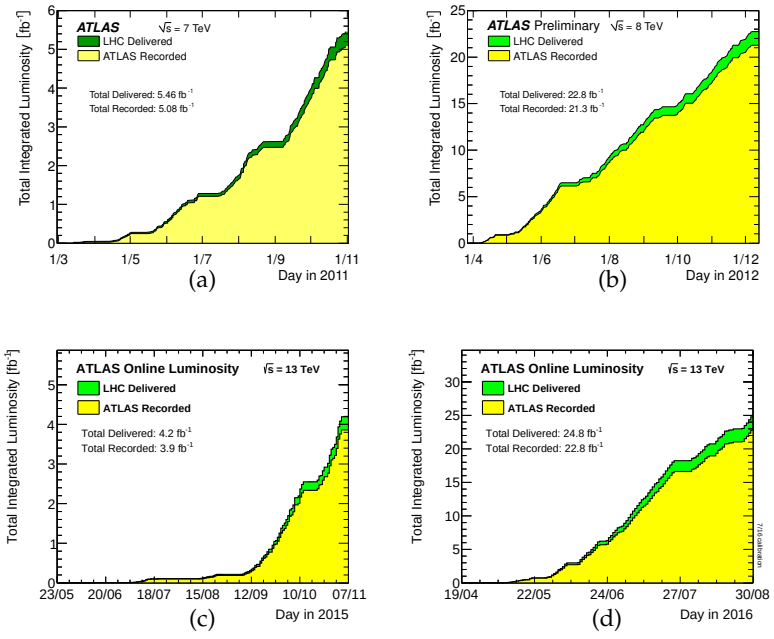

Figure 2.2: The figures show the total integrated luminosity delivered by LHC against the amount recorded by ATLAS (a) 2011 [15] (b) 2012 [15] (c) 2015 [16] (d) 2016 [17]

Rare processes like the Higgs boson where observed with this luminosity.To detect these processes in events with thousands of elementary particles, detectors who are fast responding, fine segmented and able to withstand radiation are needed. Four of these main detectors are located at the four interaction points of LHC. ALICE (A Large Ion Collider Experiment) for heavy ion collisions, LHCb (Large Hadron Collider beauty) that concentrates on matter-antimatter and the two detectors with several purposes ATLAS (A Toroidal LHC Ap-

paratus) 2.2 and CMS (Compact Muon Solenoid) who are preforming high precision measurements of the SM physics.

2.2 The ATLAS detector

With a width of $44m$, a diameter of $25m$ and a weight of about $7 \cdot 10^6 kg$ the ATLAS experiment [3] is the largest detector at LHC (see Figure 2.3). It is divided into several layers monitoring tracking, calorimetry and muon detecting. Combined with the toroidal magnet and an advanced trigger system, ATLAS is capable for dealing with the many challenges of LHC.

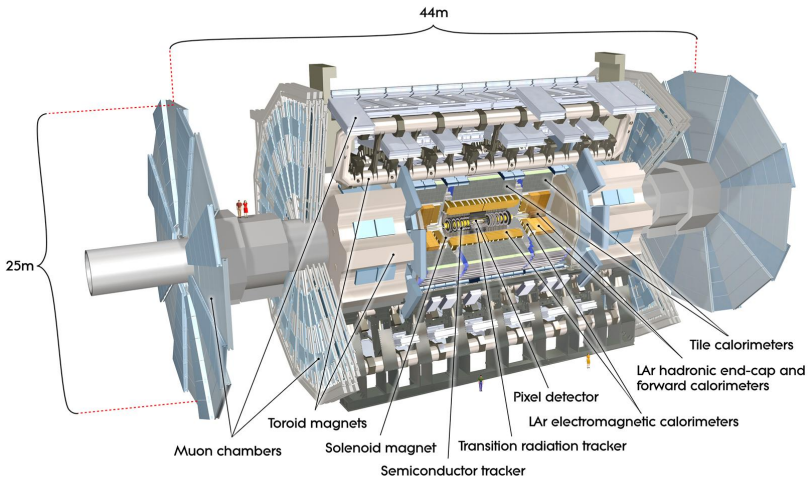

Figure 2.3: Schematic diagram of the ATLAS detector with its sub-detectors marked. From http://pages.iu.edu/~luehring/

2.2.1 Detector Requirements

The main purpose of the detector is to preform identification of experimental signatures characteristic of the physic processes, such as identifying secondary vertices or missing transverse momentum and still be able to preform excellent particle-identification. To do this in an environment like LHC with the high particle flux, fast and radiation resistance electronics and sensors are essential. Because of the nature of proton-proton collisions several proton pairs collide per interaction. To reduce the influence of these overlapping events, a high detector granularity is necessary. A large acceptance in pseudo-rapidity with almost full azimuthal angle coverage is required to detect all particles and to identify neutrinos and new particles escaping the detectors.

It is essential for the tracking system to have a good reconstruction efficiency and charged-particle momentum resolution. Tracking detectors for vertex reconstruction close to the interaction region are needed to observe secondary vertices which is used in the offline identification of τ-leptons and b-jets. The calorimeter system precisely measures the particle energy and enables the reconstruction of the

total transverse momentum. For electron and photon identification and measurements, very good electromagnetic calorimetry is required as well as full-coverage hadronic calorimetry for the jet measurements. Good muon identification and momentum resolution over a wide range of momenta is necessary. With the magnetic field the charge of muons is determined. In addition, a highly efficient triggering system is essential to achieve an acceptable trigger rate for the physic processes of interest.

2.2.1.1 Coordinate System

A common coordinate system is used throughout ATLAS. The interaction point is defined as the origin, the z-axis runs along the beam line, the x-y plane is perpendicular to the beam and is referred to as the transverse plane. The positive direction of the x-axis points towards the center of LHC and the positive direction of the y-axis points towards the surface of the earth as shown on Figure 2.4.

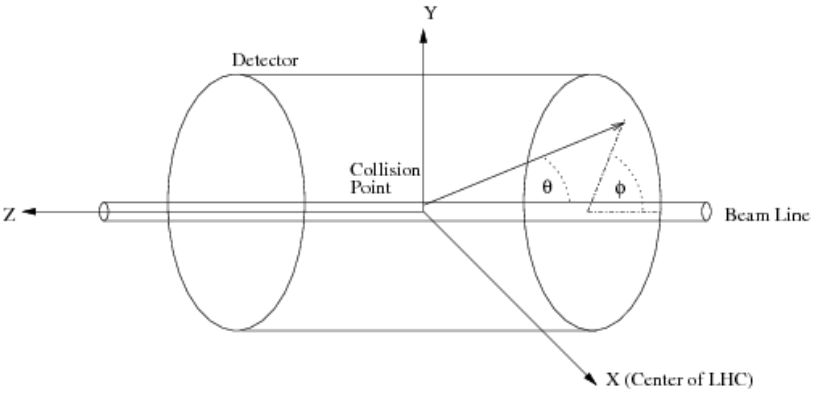

Figure 2.4: The Figure illustrate the coordinate system of ATLAS. From https://inspirehep.net/record/1294662/files/Figures_T_Coordinate.png

The particle momentum is measured in the transverse plan and is referred to as transverse momentum [P_T]. The part of the detector with positive z-values is referred to as the "*A-side*", the other half of the detector is referred to as the "*C-side*". The transverse plane is described in terms of cylindrical coordinates r and ϕ. The azimuthal angle [ϕ] is measured from the x-axis, around the beam. The radial dimension [r], measures the distance from the beam line. The polar angle [θ] is defined as the angle from the positive z-axis, it is often reported in terms of pseudorapidity, defined as $\eta = -ln\, tan(\theta/2)$.

2.2.1.2 Inner Detector

With a length of $6.2m$ and a diameter of $2.1m$, the Inner Detector (ID) is the innermost component of the ATLAS detector. It is surrounded by a $2T$ magnetic field generated by the solenoid magnet. It is designed to provide hermetic and robust pattern recognition, excellent momentum resolution and both primary and secondary vertex measurements for charged tracks above a given p_t threshold, within the range of $|\eta| = 2.5$. At each bunch crossing about 1000 particles emerge from

the collision point entering the ID, due to the large density of particles fine granularity detectors are needed to achieve momentum and vertex resolution at the required resolution.

The ID consist on three sub detectors that are put together using two technologies, silicon sensors and straw drift tubes. When a charged particle hits the silicon sensors, electron-hole pairs are generated, they can be collected by a applied electronic field. The charge is recorded locally in the sensor, identifying the position of the particle. The process in the straw drift tubes is similar to the silicon detectors. The tubes are filled with a ionized gas, and when a charged particle is traversing the tube, the liberated electrons drifts towards a wire in the center due to an applied electronic field. When the electrons hits the wire they are recorded but unlike the silicon detector, the electron traveling towards the center on the tube is amplified before detection, thus only making the measurements useful for tracking. Silicon pixels are used in the Pixel detector, silicon strips are used in the Semiconductor Tracker known as the SCT and straw drift tubes are used in the Transition Radiation Tracker known as the TRT. All the sub detectors in the ID consist of central barrel layers and end-cap disks as it is shown on Figure 2.5.

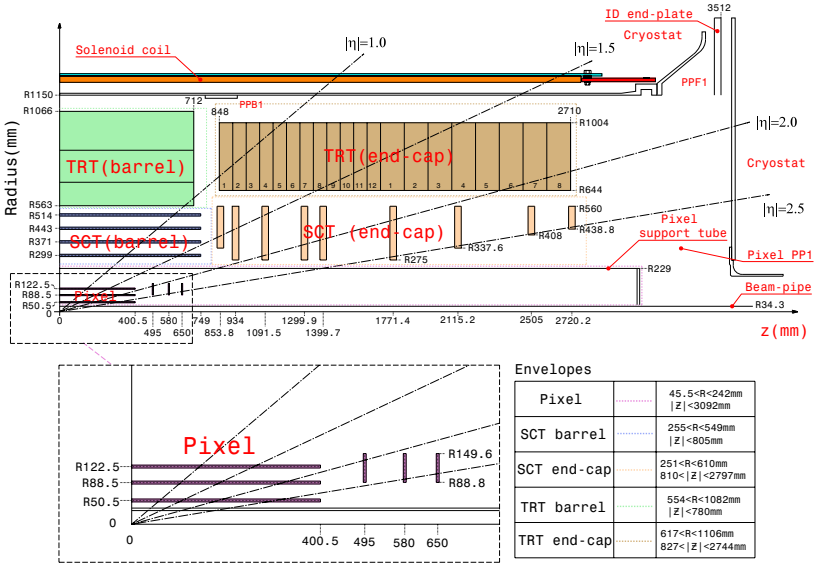

Figure 2.5: Drawing showing the sensors and structural elements of the Inner Detector (Before it was upgraded). [3]

The Pixel detector, more detailed described in section 1.2, is the sub detector closest to the interaction point and provides the highest resolution with its 1744 pixel sensors each measuring $19x63mm^2$ containing 47232 pixels on each sensor. It is divided into four barrel-shaped layers and three discs on either side. It is used for track and vertex reconstruction and b-tagging, its spatial resolution in the $r-\phi$ plane is $12\mu m$ and along the z-direction it is around $90\mu m$. The detector provides uniform coverage in ϕ and up to $|\eta| = 2.5$. How η is covered by the different parts of the Pixel Detector is shown in Appendix A.2.

The SCT surrounds the Pixel detector, consisting of four barrel

layers and nine endcaps on either side. Every layer is composed of a double layer of silicon strips, whose axes are tilted by $40mrad$ with respect to each other. The spatial resolution in the $r-\phi$ plane is $17\mu m$ and along the z-direction it is $580\mu m$. The SCT provides between four and nine measurements per particle, with the same coverage as the Pixel detector in η.

The TRT is the outermost part of the ID, it consist of 300.000 straw drift tubes providing a position measurement with an accuracy of $130\mu m$ in ϕ. On average a particle hits 35 straws for $|\eta| < 2.1$ when passing the TRT. The TRT is primarily used for tracking but can also be used for electron identification.

2.2.1.3 Calorimetry

The calorimeter system measures the deposited energy of particles by absorbing them. The system is divided into an electromagnetic and a hadronic part. The electromagnetic calorimeter is specifically designed to measure the energy of particles that interact primarily via the electromagnetic interaction. The hadronic calorimeter measure particles that interact via the strong nuclear force. Both parts are sampling calorimeters with active and passive material, to prevent the detector from becoming too large. In order to initiate a cascade of secondary particles, the passive material needs to have high density. During this particle shower low-energy particles are produced, which are then stopped and absorbed.The active material detects the shower. To measure the total energy of the initial particles, it must provide good containment for electromagnetic and hadronic showers and limit the punch-through into the muon system. In addition, a good energy resolution and a good linearity must be achieved in the measurement performance over a large energy range.

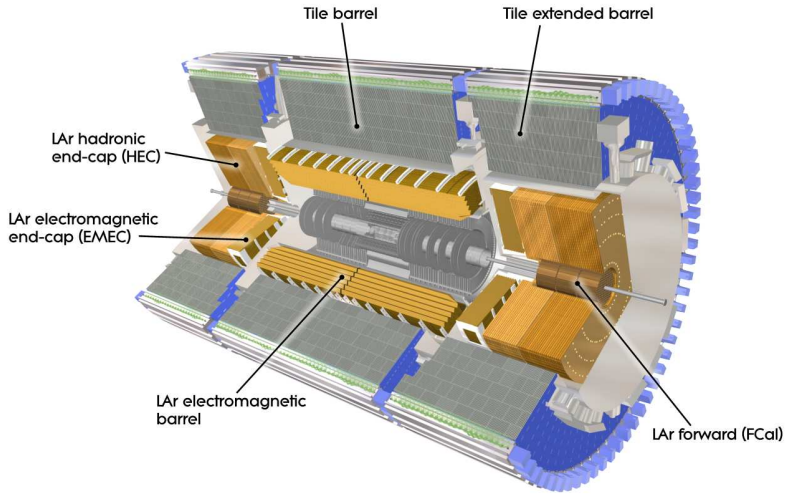

Figure 2.6: Cut-away view of the ATLAS calorimeter system. [3]

The electromagnetic calorimeter is divided into a barrel part and two end-cap components covering respectively $|\eta| < 1.475$ and

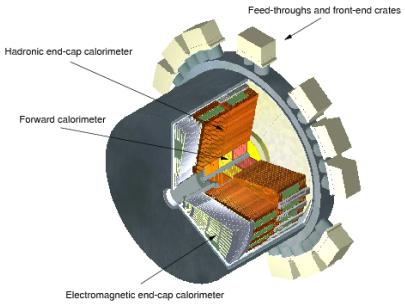

Figure 2.7: A liquid Argon end-cap cryostat, containing the hadronic and electromagnetic end-cap calorimeters, and the forward calorimeter. From https://inspirehep.net/record/1211185/files/LARG2-endcap_cryostat.png

$1.375 < |\eta| < 3.2$, each housing their own cryostat. It measures the energy of electrons and photons. Photons does not interact with the tracking detector, so their directions is only determined by the point of impact in the calorimeter. Liquid Argon is used as active material with accordion-shaped kapton electrodes and lead absorber plates over its full coverage.

The hadronic calorimeters detects all hadrons using different techniques suited for the widely varying requirements. The tile calorimeter is placed directly outside the electromagnetic calorimeter as shown in Figure 2.6. Its barrel covers $|\eta| < 1.0$ and then it has two extended barrels covering the range $0.8 < |\eta| < 1.7$. It uses steel as absorber and scintillating tiles as the active material. The Hadronic End-cap Calorimeter (HEC) covers the higher pseudorapidity region $1.5 < |\eta| < 3.2$, it is located directly behind the end-cap electromagnetic calorimeter and shares the same LAr cryostats but uses copper as absorber. To reduce the drop in material density at the transition between the end-cap and The Forward Calorimeter (FCal) around $|\eta| = 3.1$, the HEC extend out to $|\eta| = 3.2$ thereby overlapping the FCal. The FCal is integrated in into the end-cap cryostates, since this provides benefits in terms of uniformity of the calorimetric coverage and a reduced level of background radiation in the muon spectrometer. It covers the high pseudorapidity regions of $3.1 < |\eta| < 4.9$ and consists of three modules in each end-cap: the first, made of copper, is optimized for electromagnetic measurements, while the other two, made of tungsten, measure predominantly the energy of hadronic interactions. Each module consists of a metal matrix, with regularly spaced longitudinal channels filled with the electrode structure consisting of concentric rods and tubes parallel to the beam axis.

2.2.1.4 Muon system

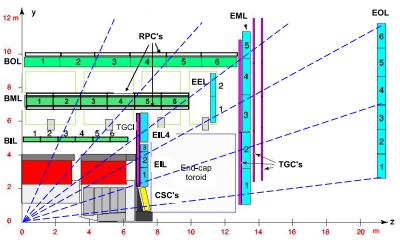

Figure 2.8: Initial configuration of the muon spectrometer with its four chamber sub-systems: the precision-measurement tracking chambers (MDT's and CSC's) and the trigger chambers (RPC's and TGC's). [3]

The muon spectrometer is the outermost part of the ATLAS Detector marked with a light blue color in Figure 2.3 and since all other known particles, except neutrinos, is stopped in the calorimeter, only muon reaches this part. The muon spectrometer has two functionalities; fast triggering of muons originating from the interaction point, and high precision measurement of the momentum. The muon measurements is based on magnetic deflection of the trajectory of the muons by the large superconducting air-core toroid magnets, whose field reach out to $|\eta| = 2.7$. The magnetic field in the barrel region has a value of $0.5T$ on average and can reach $3.5T$ in the end-cap region.

Due to the different detector environments in ATLAS it is a diverse task to trigger and track muons and to manage this four types of detectors is present. The triggering detectors is very fast and has a good time resolution. The tracking detectors has a good spatial resolution to measure the bending of the particle trajectory in the magnetic field. Due to the higher particle flux close to the beam pipe at high η different detectors are needed here.

Resistive Plate Chambers (RPC) are used for triggering in the central region at $|\eta| < 1.05$. RPCs are finely segmented gaseous parallel electrode-plates, operating in "avalanche mode" and having an intrinsic time resolution of $1.5ns$. The Thin Gap Chambers (TGC) in the forward regions at $1.05 < |\eta| < 2.7$ are multi-wire proportional chambers. They can cope with higher counting rates, but have an intrinsic time resolution of $4ns$. In addition to triggering, the RPCs and TGCs are also used to provide tracking information. Drift tubes filled with an Ar/CO_2-gas mixture, which are called Monitored Drift Tubes, are used in the barrel region $|\eta| < 2$ for high resolution tracking with a stand-alone spatial resolution of $35\mu m$. Cathode Stripe Chambers (CSC), which are multi-wire proportional chambers with strip cathodes, are utilized in the region $2 < |\eta| < 2.7$ having a spatial resolution of $40\mu m$.

2.3 Silicon Detectors

Creation of electron-hole pairs from a passing ionizing particle is the basic principle of a semiconductor detector. A charge carrier induce a signal, when drifting in an electric field towards the electrode. Since silicon detectors fulfill all the requirements listed in Section 2.2 low material cost, the possibility of fine segmentation and the ability to measure close to the particle beam, it is a commonly used material when designing semiconductor detectors.

2.3.1 Properties of Silicon

In energy-band theory, a material is described by introducing a valence band and a conduction band. Electrons in the conduction band can move freely in the atomic lattice, while electrons in the valence band (valence electrons) are bound to individual atoms. The Energy Band Gap E_g between these two bands define the materials conductivity. An insulator has a large gap between the bands, usually larger than 3 eV shown in part (a) of Figure 2.9. In metal these two bands overlap resulting in a good conductivity, part (c) of Figure 2.9, and in a semiconductor the band gap is smaller than 3 eV, as a result only a small amount of energy is needed to "free" an electron and carry a charge, the semiconductor band setup is shown in part (b) of Figure 2.9 [18].

For silicon the $E_g = 3.62$ eV making it a indirect semiconductor. E_g of silicon is 10 times smaller than the energy required for gas ionization [19].

The signal charge Q of a m.i.p. is given by [20]

$$Q = \frac{\langle \frac{dE}{dx} \rangle \rho d}{I_0} \tag{2.4}$$

With the density silicon $\rho = 2.329\text{g cm}^{-3}$ and the sensor thickness in the ID $d = 250\mu m$, the average charge is $Q = 24000e$ or $29 \cdot 10^3$ electron-hole pairs, this charge is sufficient to be processed. However,

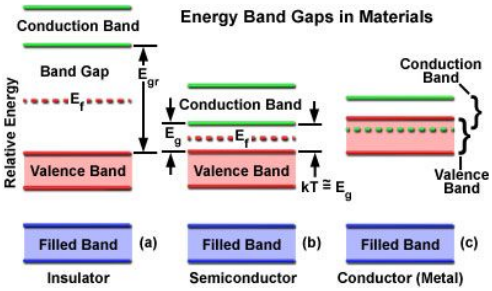

Figure 2.9: Description of the electronic bands in solids. []

in order to detect such charge, the electron-hole pairs created by the thermal charge carriers must be depleted. The density of intrinsic free charge carriers at room-temperature is $9.65 \cdot 10^9$ cm^{-3}, which means that in a $50\mu m \times 400\mu m$ pixel about $5 \cdot 10^7$ free electrons exist [21]. Thus, pure silicon is not suitable as sensor material.

2.3.2 pn-junctions

Instead of using pure silicon, a modulation is needed. To fine-tune silicon and other semiconductors electrical properties, a method where the material is intentionally impurified called doping. There are two types of doping, either an extra valence electron is added called donor or a valence electron is removed called acceptor. In case of silicon which is a group four (IV) element, a donor would be an atom from group five (V) and an acceptor atom would be an atom from group three (III).

The donor atom adds states closer to the conduction band, electrons in these added states are easier to excited since E_g is smaller. In the opposite case of acceptor atoms, holes are made, which refers to new unoccupied states in the valence band. Referring to their overall charge, semiconductors with donors are called n-type and semiconductors with acceptors are called p-type. The idea of doping is to make the concentration of additional electrons or holes big enough to make them the most important charge carriers [22].

By combining p-type and n-type silicon it is possible to produce a sensor with a low concentration of free charge carriers, this is called a pn-junction. At the junction the concentration difference results in a diffusion of the respective majority charge carriers. This diffusion process is compensated by an electric field caused by the remaining space charge. An equilibrium configuration is reached and the pn-junction region is depleted for free charge carriers [4].

The width of the depleted zone d and the number of electron-hole pairs contributing to the signal is increased by applying a bias voltage U_{bias}, given by [24]

$$d = \sqrt{\frac{2\epsilon\epsilon_0}{N_D e} U_{\text{bias}}} \tag{2.5}$$

where N_d is the donor concentration. It is optimal if the depleted zone stretches over the whole sensor area, the U_{bias} needed to obtain this is called referred to as the depletion voltage, as the sensor material is depelted of free charge carriers when this voltage is applied.

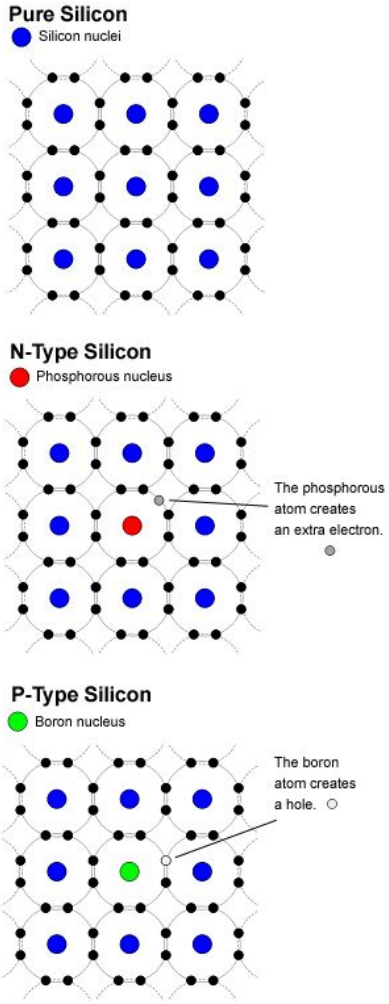

Figure 2.10: Description of the electronic bands in solids. [23]

2.4 Output from hits

When a detector gets a signal, a discriminator is used to verify if the signal is large enough to originate from a particle hit. This is a way to reject some of the noise hits early on in the process, reducing the amount of data handling later on.

If the discriminator gets a signal with a well controlled shape and a rise-time[1] significantly shorter than the falling edge[2], the time the

[1] The time it takes the signal to reach its maximum.
[2] The time is takes the signal to fall below the threshold from its peak

signal remains above the threshold (referred to as time-over-threshold or ToT) relates to the charge of the particle hitting the detector. The ToT is measured by determining the time difference between the rising and falling edges of the discriminator output.

A concern when a hit is measured by the discriminator, might be the presences of time-walk if the particle is of low charge. Time-walk is illustrated in Figure 2.11. If the time-walk is too large, the hit might be detected too late and thereby be associated to a bunch-crossing or trigger later than the hit actually occurred. This is adjusted by the setting of the amplifier supply current and is a compromise between power consumption and thus heat dissipation and the need to keep the time-walk as small as possible.

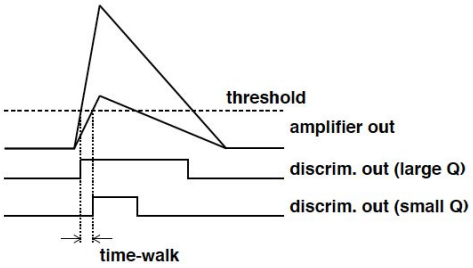

Figure 2.11: Amplifier output and discriminator response for a small and a large charge signal on the amplifier input. [4]

2.5 Track Reconstruction

Due to the high track density, several collisions in each bunch crossing[3], the need to cover all particle momenta and direction in a environment with unavoidable amount of passive material, data recording in hadron collider experiments are a very complex matter [25]. To manage this task highly evolved track finders and fitters are needed.

2.5.1 Detector Element to Space Point

A hit is when a electron cloud induce a signal on pick-up electrodes in a detector element. If the signal is only induced on one electrode, the space-point precision is $\Delta/\sqrt{12}$, where Δ is the electrode size. A better precision is possible if the signal from the hit is distributed over two or more electrodes, in that case it is possible to determine the space-point very accurately. If the signal is distributed over several electrodes, the barycenter[4] is given by

$$x = \frac{\sum x_i P_i}{\sum P_i} \tag{2.6}$$

Where P_i is the pulse heights on the electrodes. The barycenter is a popular estimate of the space-point [25].

Due to the finite size electrodes, this estimate has a bias for purely geometric reasons[5], but this bias can be corrected for.

[3] Known as pile-up

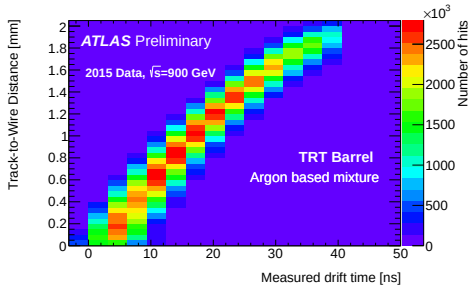

Figure 2.12: This plot shows the TRT R-t dependency for the TRT barrel as obtained from 900GeV collision data with all TRT straws filled with Argon gas. This relation is used to infer track to wire distance, i.e., drift radius, based on measured drift time. [26]

[4] the point between two objects where they balance each other; it is the center of mass where two or more bodies

[5] The bias is largest for true impacts half way between the edge and the middle of the electrode

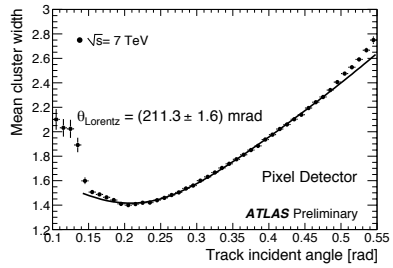

Figure 2.13: Pixel cluster width as a function of the track incident angle in $R\phi$ direction. x-axis corresponds to the track incidence angle on the pixel module ($R-\phi$ plane) in local reference frame. Only clusters on tracks are considered. [27]

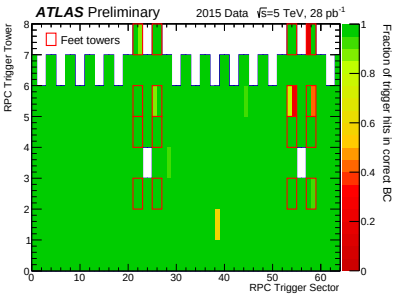

Figure 2.14: Fraction of RPC trigger hits associated correctly to the collision Bunch Crossing for each of the 428 Barrel Muon trigger towers.One tower with hardware problems (Tower = 2, Sector = 38) is visible as an orange area. The two white areas (Tower = 3, Sector = 23, 24, 55, 56) correspond to the "elevator" chambers, not yet commissioned in 2015. Data from pp runs at $\sqrt{s} = 5$TeV, integrated luminosity $L = 28\text{pb}^{-1}$. [28]

2.5.1.1 Calibration

To reconstruct a space-point correct, the probability distribution of induced pulse heights for a given track impact on the surface of a detector module, also called the response function, must be known. This function can be measured with test beam probes and with real data themselves. Due to vary from channel to channel and even variation over time in a given channel, a continuous calibration of all the individual response functions must be carried out during data taking. Some of the examples of response functions and their parameters are:

R-t dependency is the relation between the distance from the track to the wire is a drift tube R and the measured drift time t. To establish this relation in a drift tube, R is plotted against t as shown in Figur 2.12 and a function $R(t)$ is fitted to these data.

Lorentz angle is the angle between the electric field and the direction of the drift of the electron and holes in a silicon strip or pixel detector, when submerged in a magnetic field. The cluster size is plotted against the incident angle of the track and the angle at minimum size is found as shown in Figure 2.13.

Pedenstal is the electronic noise level in each channel, it is determined by reading out the detectors when the collider is turned off. Noise from the beam can be measured by recording a unpaired beam passing through the detector.

Dead or noisy channels are located by finding peaks or holes in a histogram of hit channels filled during a run, as shown in Figure 2.14 where the yellow rectangle shows a misreading pixel. Such a channel should be ignored, but their presence still taken into account in clustering algorithms.

2.5.2 Measuring Momentum

A moving charged particle will be bend by the Lorentz force when exposed to magnetic field, the bending will take place in the plane perpendicular to the field. If the field is homogeneous the radius of the curvature can be used to calculate the particles momentum transverse to the field, the transverse momentum p_T is given by

$$p_T = qB\rho \tag{2.7}$$

or

$$p_T\ (\text{GeV}/c) = 0.3B\rho\ (T \cdot m) \tag{2.8}$$

Where q is the charge of the particle, B is the magnetic field and ρ is the radius of the curvature. Equation 2.8 is the basic equation of a spectrometer, in the case of ATLAS it has to be modified since the track of a particle will be known by points and not by a full track.

In 3D the particle trajectory will be a helix. Let us assume a field confined to the stretch, L, shown on Figure 2.15. The momentum projected on the bending plane can be found by a measurement of the bending angle, θ, or alternatively of the sagitta, s, of the trajectory piece of arc inside the field region. The use of the sagitta is as follows [25]:

$$\frac{L}{2\rho} = \sin(\theta/2) \approx \theta/2 \rightarrow \theta \approx \frac{0.3L \cdot B}{p_T} \tag{2.9}$$

$$\Delta p_T = p_T \sin\theta \approx 0.3L \cdot B \tag{2.10}$$

$$s = \rho(1 - \cos(\theta/2)) \approx p\frac{\theta^2}{8} \tag{2.11}$$

$$s \approx \frac{0.3}{8}\frac{l^2 B}{p_T} \tag{2.12}$$

With this knowledge let us look at a particle detector with three measurement stations inside the magnet: One at the entrance, one in the middle and one at the exit. All stations measure the coordinate x of the particle with a resolution of $\sigma(x)$. Thus the estimate of the sagitta is:

$$s = x_2 - \frac{x_1 + x_3}{2} \tag{2.13}$$

the resulting relative uncertainty on the measured momentum is then:

$$\frac{\sigma(p_T)}{p_T} = \frac{\sigma(s)}{s} = \frac{\sqrt{\frac{3}{2}}\sigma(x)8p_T}{0.3 \cdot BL^2} \tag{2.14}$$

where again p_T is in GeV/c, B is Tesla and L in meters.

Looking into eq. 2.14 it is clear that the 'lever arm' L is the most important parameter, followed by the position resolution $\sigma(x)$ and the strength of the field B. It is also clear that the relative momentum uncertainty due to measurement resolution, will increase linearly with the momentum.

Furthermore eq. 2.14 shows that the number of space-point measurements enters only with a square root in the momentum resolution, another reason not to add too many measurement stations is the additional material in the path of the charged particle. This additional material will lead to further multiple scattering which will smear the particle direction and contribute to the uncertainty in the transverse momentum. A spectrometer with the length L, made of a material with radiation length X_0 the contribution to the uncertainty will by [25]:

$$\Delta p^{MS} = p\sin(\theta_{MS}) \approx p \cdot 0.0136\frac{1}{p}\sqrt{\frac{L}{X_0}} \tag{2.15}$$

again with p in GeV/c.

The particle receives a 'p_T-kick' from the magnetic field equal to:

$$\Delta p_T = 0.3 \cdot BL \tag{2.16}$$

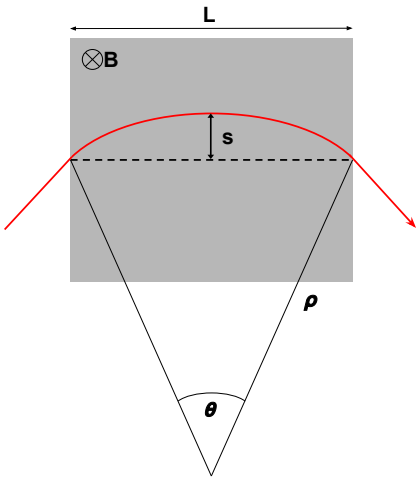

Figure 2.15: The momentum projected on the bending plane can be found by measuring the sagitta s, of the trajectory piece of arc inside the field region.

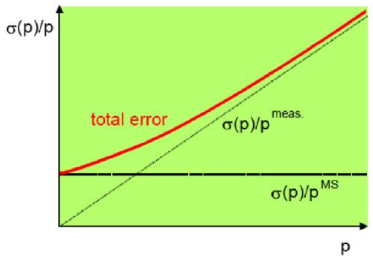

Figure 2.16: The graph shows the contribution from measurement resolution and multiple scattering to the total uncertainty as a function of the momentum, p.
.[25]

and the relative momentum uncertainty due to multiple scattering is [29]:

$$\frac{\sigma^{MS}(p_T)}{p_T} = \frac{\Delta p^{MS}}{\Delta p_T} = \frac{0.0136\sqrt{\frac{L}{X_0}}}{0.3 \cdot BL} = 0.045\frac{1}{B\sqrt{LX_0}} \tag{2.17}$$

The most interesting point here is that this contribution to the uncertainty is independent of p.

As illustrated in Figure 2.16 the uncertainty is dominated by multiple scattering at low momentum and by measurement errors at high momentum. In the Inner Detector of ATLAS the transition happens at a transverse momentum of around 30 GeV/c [25].

2.5.3 Track Parameters

Track reconstruction is the function of finding the collection of hits created by passage of each track and use these to estimate its track parameters.

A charged particle in a homogeneous magnetic field, will from the equation of motion have a trajectory of a helix, characterized by the radius, R, the position at an arbitrary point of the helix (X_0,Y_0,Z_0), the tangential direction at the same point given by the angle λ and α_0 and a sign h indicating which way the particle moves. Moving along the helix away from the initial position by the path length, s, we trace out the positions [25]:

$$\begin{pmatrix} x \\ y \\ z \end{pmatrix} = \begin{pmatrix} x_0 + R \cdot \cos((\alpha_0 + \frac{hs}{R} \cdot \cos\lambda) - \cos\alpha_0) \\ y_0 + R \cdot \sin((\alpha_0 + \frac{hs}{R} \cdot \cos\lambda) - \sin\alpha_0) \\ z_0 + s \cdot \sin\alpha_0 \end{pmatrix} \tag{2.18}$$

The helix parameters could be chosen differently and a particular point could be chosen as a starting point. A often used choice is the perigee parameters, here the perigee is the point on the helix closest to the beam-axis. The parameters are the signed distance of closest approach, d_0, the coordinate along the z-axis at this point, z_0, the azimuthal angle of the tangent at this point, ϕ_0, the polar angle of the track to the z-axis,θ and the charge over momentum, q/p. Given the vector [25]:

$$\bar{x} = (d_0, z_0, \phi_0, \theta, \frac{q}{p}) \tag{2.19}$$

This vector is called the state vector of the track at the perigee.

The beam axis is a particular choice. It can be replaced by an axis of a detector element and quote the state vector with respect to this axis. One can say that a track is a collection of state vectors, supplemented with their covariance matrices, one for each of the detector surfaces where the track has an associated hit. In the end, however, it is the track state at its production vertex which are the parameters of the interest [25].

III The Analysis

3.1 Data Samples and Event selection

3.1.1 Charge of Clusters

As described in section 2.4 a m.i.p. crossing a silicon pixel sensor will generate ≈ 80 electron-hole pairs per micrometer of thickness [1]. The calibration of the detector is such that a m.i.p. crossing a sensor of the thickness $250\mu m$ at normal incidence angle will give a ToT count of 30, while the overflow is at 255. Each pixel diode will measure a charge ranging from $3.5ke$ to $170ke$. All Pixel Read-out channels are calibrated and equalized within 2% [1], which is significantly below the intrinsic accuracy of the ionization loss for a m.i.p. The charge collection efficiency is uniform over the sensor area with the exception of dead areas which is estimated to $\approx 3\%$, most of the dead areas is due to non operational Pixel modules. The fraction of individual dead pixels is only a few per mil [1]. When a track is crossing the Pixel Detector the charge generation is rarely contained within one pixel. The charge generation often happens in neighboring pixels that forms clusters and the charge of the cluster is calculated by summing up the charges of all the pixels after calibration corrections. This way of measuring the charge in the Pixel Detector can be biased for various reasons.

(a) Foremost some charge may be lost due to the $3.5ke$ threshold, this will mainly occur in the outskirts of a cluster.

(b) Charge is also lost if the cluster is located at the boundary of a dead region or of the module.

(c) In rare cases the charge in a pixel may be lost because the ToT counter of a given pixel exceeds 255.

(a) and (c) are unavoidable biases while (b) can be removed by fiducial volume cuts.[]

3.2 Good Cluster

A Good Cluster (GC) is defined to remove hits in regions of the ID that could provide misleading read-outs from tracks, in this case Good Clusters will mainly be defined by their credibility in relation to the charge read-out.

In earlier analysis [1] cuts as mentioned in the above sections has been made to reducible the biases indicated, by applying constrains on the local position in the x-direction of the cluster to neglect clusters at the edge of the module, i.e. the $\approx 1mm$ region along x between two facing read-out modules.

In my analysis I studied if the clusters location on the pixel module might influences the charge read-out. I expected to see a drop in the charge measured at the edges of the modules since cut in earlier analysis where made here. I divided the analysis into three sections the IB layer, the barrel layers and the end-caps. The IB layer (IBL) were

handled alone since the dimensions of its pixel modules is different from the rest of the ID and since the IBL is an update inserted later than the rest of the ID, the technology in the modules is therefore most likely different. The barrel and end-cap were divided primarily because they are located differently in the ID, but also because the individual pixel modules are located different in respect to each other, respectively forming a cylinder and a disk which might influence the charge read-out, therefore these are analyzed individually as well.

First of all I made sure that the clusters were evenly distributed throughout the pixel modules and no cuts where needed. To do this I plotted the localX variable Vs. the localY variable, these variable are coordinates of the clusters positions on the individual pixel module. If any systematic error on the position read-out should be present an uneven distribution would appear from the plot shown in Figure 3.1, as seen in the figure the distribution of the clusters is even throughout the modules.

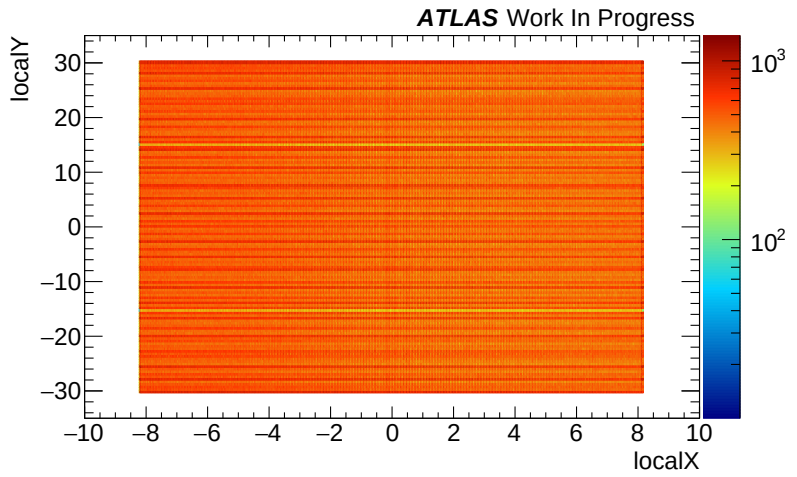

Figure 3.1: The plot shows the distribution of the cluster locations on the barrel pixel modules. The distribution can be considered even since the checkered pattern originate from ROOTs drawing and alters when you change the since of the figure.

As there are no further to take into account with respect to the uniform distribution of the clusters at the pixel modules, the next interesting study would be to compare the charge read-out with the location of the cluster. First of all to locate the reason of the cut mentioned in the beginning of this section, a drop in charge should be seen at the edge of modules. To search for this plots of both the local position in the x and y direction are plotted against the charge read-out, as shown i Figure 3.2 and 3.3.

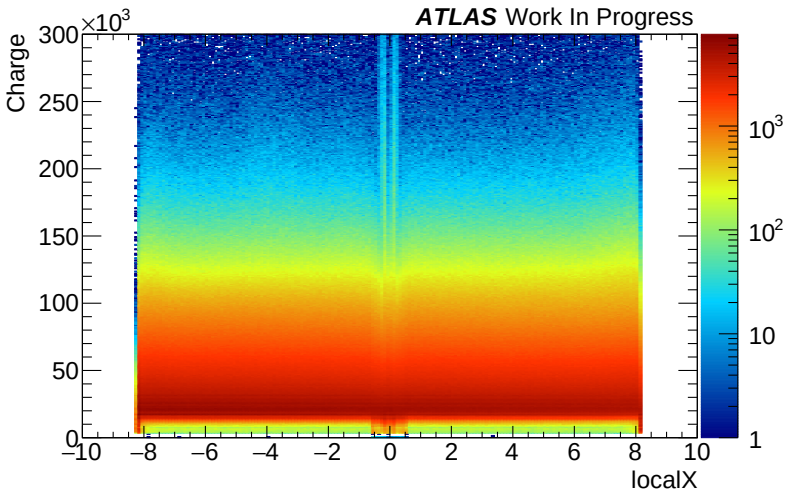

Figure 3.2: This plot is a 3d histogram, on the x-axis is localX which is a variable referring to the position on the detector modules x-axis. On the y-axis is the charge read-out value for a given cluster. This plot visualize the distribution of the charge measurements for a given location on the x-axis, this is used to locate areas that returns unreliable information.

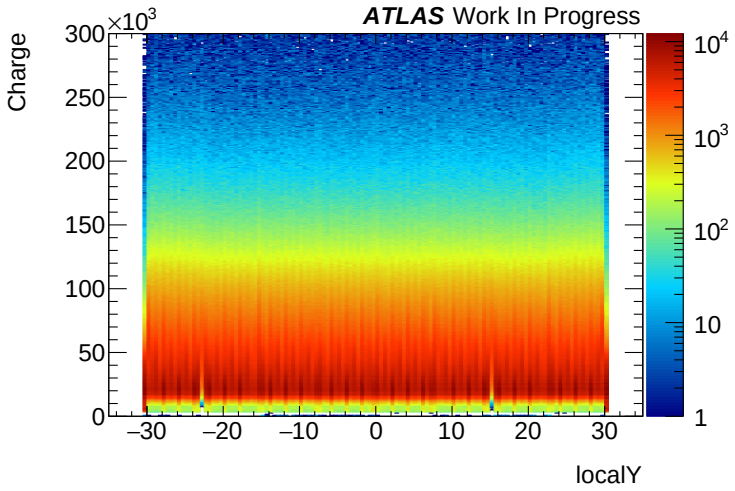

Figure 3.3: This plot is a 3d histogram, on the y-axis is localX which is a variable referring to the position on the detector modules x-axis. On the y-axis is the charge read-out value for a given cluster. This plot visualize the distribution of the charge measurements for a given location on the y-axis, this is used to locate areas that returns unreliable information.

Looking at Figure 3.2 starting with the edge it clear that some inconsistency is present, focusing at the left edge as shown in Figure 3.4 is it easy to see that the peak of the charge read-out has shifted to a lower value, the edge effect observed in earlier analysis are definitely still present. Before defining a cut to remove the clusters too close to the edge of the module, another thing that catches my eye in Figure 3.2 is the charge read-out tail symmetrically distributed around the center of the module, that also seems to shift the peak of the charge and could be due to the instrumental setup on the pixel module. To see the effect of this and likely make some cuts to remove this effect, a TProfile plot in ROOT that replaces each charge bin with the average of the bin, as shown in Figure 3.5. To define any cuts it is important vary the binning of the x-axis and study the difference in result, a low binning would result in a misleading uniform distribution where areas with deviations in the charge read-outs would be smeared out and not be detected, in contrast a high binning would risk to empty bin that are not directly hit but still located in a fully functional region. I only want to cut away regions that are generally throughout all pixel modules returning misleading read-outs. In the case of localX I choose 600 bins corresponding to 10 bins per mm.

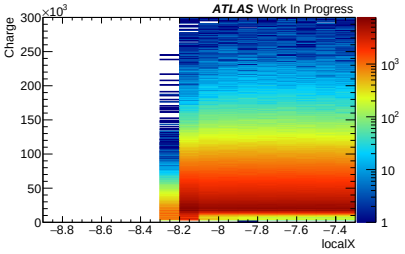

Figure 3.4: This is a zoom-in on the left edge of Figure 3.2. Close to the edge a the average of the charge read-out drops, which make measurements close to the edges unreliable.

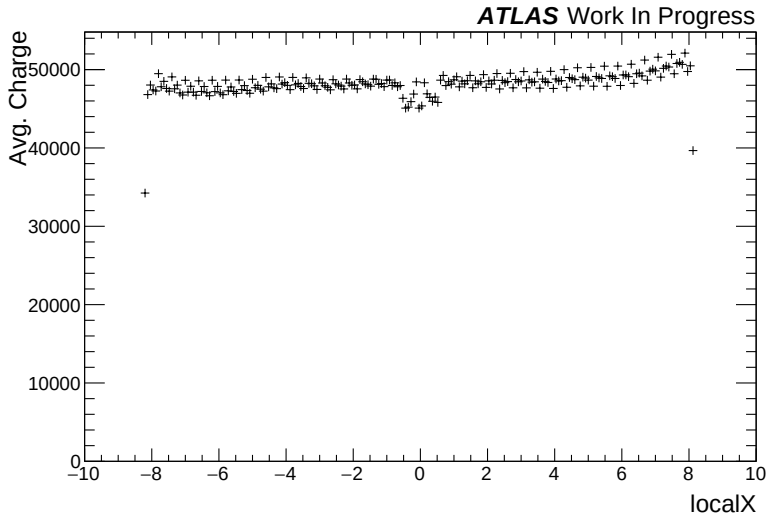

Figure 3.5: This plot is a *Profile* plot of Figure 3.2, used of define when exactly the charge read-out should be excluded.

When the binning were decided next step was to define which regions to remove from data by applying the cuts in localX. It clearly appears that the charge is misread at the edges close to localX $= 8$ and -8, I chose the edge-cut so that clusters within $localX = [-8.05; 8.05]$ would be included reorganized as a GC. A more challenging cut to make was in the middle region, as this region only shifts the charge read-out by a small amount. I chose to cut this middle region away since the $TProfile$ plot in Figure 3.5 clearly shows a discontinuance in the average charge, the center cut were therefore defined to exclude all clusters within $localX = [-0.325; 0.300]$. The same steps were made in the y-axis of the pixel module shown in Figure 3.3 where

no discontinuances were found within the module, only the edges needed to be removed by requiring that $localY = [-30.0; 30.0]$. The same procedure as described for the barrel region was made for both IBL and the Endcap to define cuts for their pixel modules too. These cuts and the clusters affected by them can be seen in Table 3.1 and the plots used can be seen in Appendices A.3. The total amount of clusters that will not be accepted as GC's is 7%, the amount of clusters affected by each cut is noted in Table 3.1.

Table 3.1: The table show the cuts applied to the clusters $localX$ and $localY$ value. [.;.] are values that the variables should be within and].;.[are intervals that the variables should not contain. The first column contains the flags that a cluster get in the goodCluster variable made from these cuts, at variable used to separate GC from other clusters in this variable a GC would have the value 0. The last column contains the number of cluster flagged by the cut and the ratio compared to the total amount hits in ID. The total amount of hits that wont be accepted as a GC is 7% of the total number of hits.

Flag	Position	Cut		#Cluster Affected
			Total hits	2.366.001.383
			Total Barrel Hits	1.488.703.298
1	Barrel Center	$localX =$	$]-0.325; 0.300[$	56.997.637
2	Barrel X Edge	$localX =$	$[-8.05; 8.05]$	30.265.675
4	Barrel Mid			
8	Barrel Y Edge	$localY =$	$[-30.0; 30, 0]$	29.130.442
			Total Endcap Hit	325.949.459
1	Endcap Center			
2	Endcap X Edge	$localX =$	$[-8.15; 8.13]$	2.518.323
4	Endcap Mid	$localY =$	$]-23.0; -22, 5[+$ $]15.0; 15, 5[$	6.228.808
8	Endcap Y Edge	$localY =$	$[-30.0; 30, 0]$	5.393.534
			Total IBL Hit	551.348.626
1	IBL Center			
2	IBL X Edge	$localX =$	$[-8.35; 8.35]$	3.407.830
4	IBL Mid	$localY =$	$[-0.5; 0, 5]$	13.493.096
8	IBL Y Edge	$localY =$	$[-20.1; 20, 1]$	10.195.970
			Total Hits Affected	155.758.318

The Flag mentioned in Table 3.1 is the the number a cluster get in its goodCluster variable if it is flagged by a certain cut. As an example if a given cluster is inside the Barrel Center cut its goodCluster value will be 1, if it at the same time is outside the Y edge cut 8 would be added to the value at the cluster goodCluster value will be 9. By doing it this way it is possible to filter in which cut should be applied in different analyzes without the need of a new dataset.

3.2.1 Charge vs. cos(α)

Due to the different orientation of the modules relative to the magnetic field in the barrel and in the endcap regions of the ID the Lorentz angle effect requires to be taken into account when making geometrical cuts [1], to do this the dependency of the most probable value of the charge were tested against α, where α is the spatial incident angle calculated versus the normal to the surface of the module.

Since charge for a given α is a distribution shown in Figure 3.6, to find the most probable value of the charge fitting is necessary. I sliced the the x-axis into 100 1D histogram one for each cos(α)= 0.01 for each of these histograms I used the ROOT function $GetMaximum()$

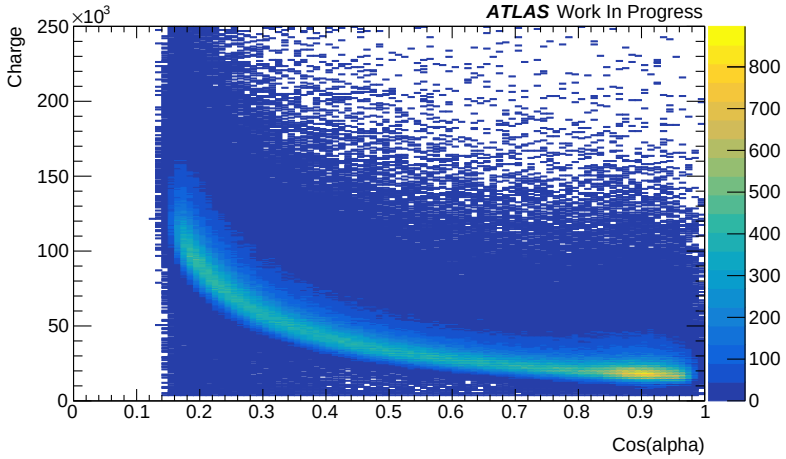

Figure 3.6: Charge of clusters against α the angle to the normal of the surface of the modules, in this case for the first barrel layer (black) and the IBL (blue). Both following the same function, the shift between the two layers is due to the IBL have thinner detectors than the rest of the ID.

to find the bin with the highest value and then I fitted a Gauss to the backside of the peak and a Landau distribution to the front side[1]. The parameters from these fits, are then used to fit a Gauss+Landau function for the full range of charge distribution, four examples from the first barrel layer of these fits are shown in Figure 3.7.

[1] I defined the front side as the right side, with the long tail

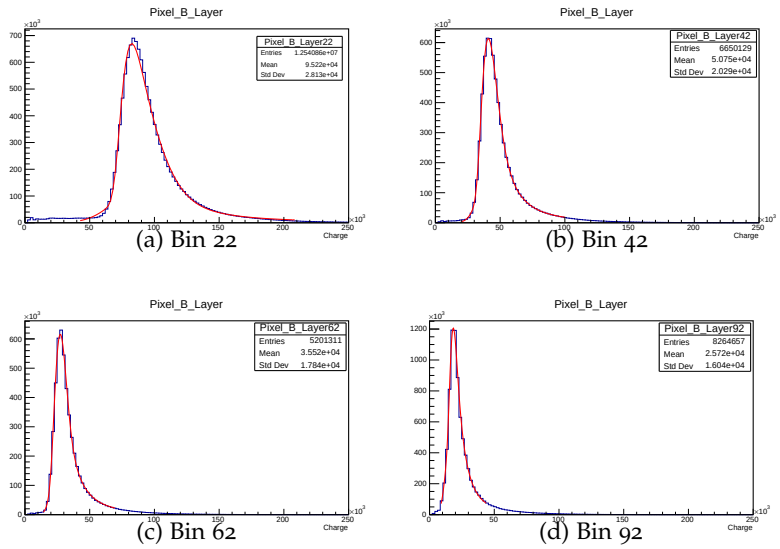

(a) Bin 22 (b) Bin 42

(c) Bin 62 (d) Bin 92

Figure 3.7: The histograms show the effect of the cut, made in Table 3.1, on the average number of hits per track.

I did this fitting for each layer in the ID to make sure that the dependency were the same in all layers, for the IBL I did three fits since this layer consists of three individual parts [2]. Figure 3.8 shows the dependence of the most probable value of the charge on $\cos(\alpha)$ fitted with the simulation used in earlier analyzes [1]. Despite outlayers which originates from fits that failed (example shown in Figure 3.9) and the low statistics in lower values of $\cos(\alpha)$, the tendency shows good agreement with the simulation. The fact that the points are divided in two lines, is a result of the difference in the thickness of the pixel detectors in the IBL and the rest of the ID. Since a thinner detector for a given dE/dx results in a lower charge read-out.

[2] The 3D_plus, the planar and the 3D_minus

Another application of the plot in Figure 3.8 is to study if any cuts in $\cos(\alpha)$ are needed, earlier analysis [1] showed that clusters below $\cos(\alpha) > 0.16$ had a misalignment with the simulations and was therefore removed. I haven't been able to locate this misalignment down to $\cos(\alpha) = 0.12$ and below this point statistics in my data high enough to fit the charge distribution, therefore no cuts is applied here.

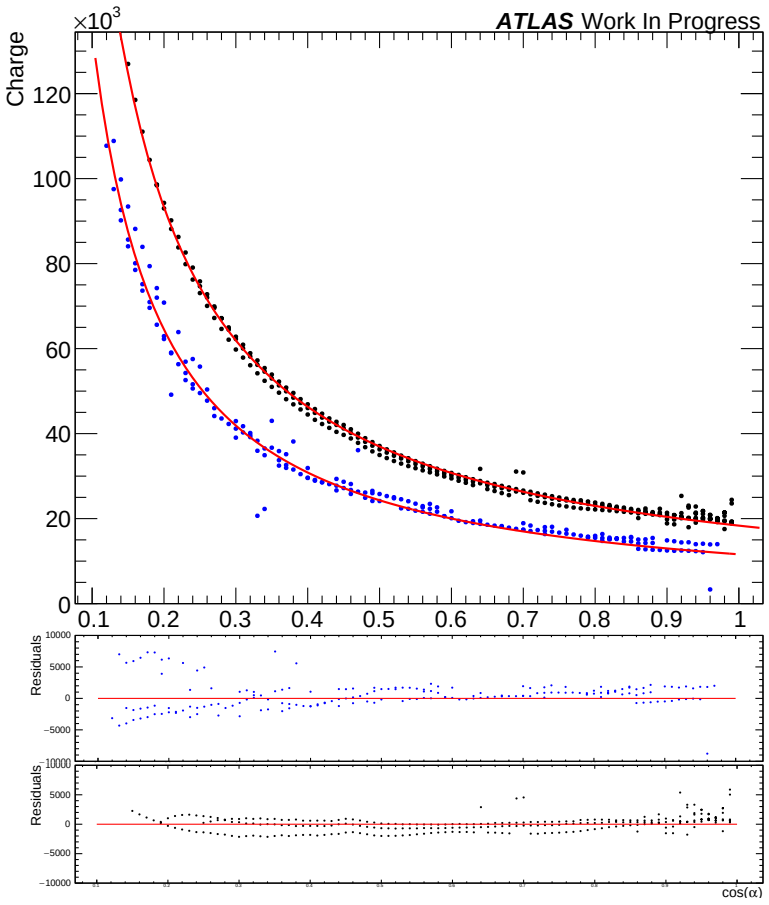

Figure 3.8: Charge of clusters against α the angle to the normal of the surface of the modules, in this case for the first barrel layer.

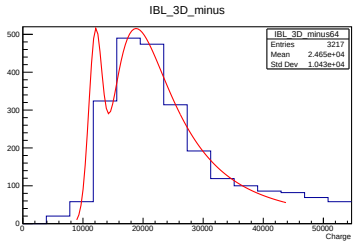

Figure 3.9: An example of a failed fit from the process shown in Figure 3.7, that still gets plotted as a point in Figure 3.8. These failed fits explains most of the out-layers in Figure 3.8.

3.2.2 Effect of selection cuts

The effect of the cluster selection cuts on the number of hits used to calculate dE/dx of each track for both data and Monte Carlo can be seen in Figure 3.10. The green histogram shows the result when no cuts are made at all, the yellow shows the result with the cuts I made and the black bars with a dot in the center shows the result using the cut in earlier analyzes [1]. What I did not expect was to see that the old cuts actually removed more hits than the new once I made. The explanation to this could be the extensive cut in the localX only including hits inside $[-7.15; 7.15]$ compared to my cuts shown in Table 3.1.

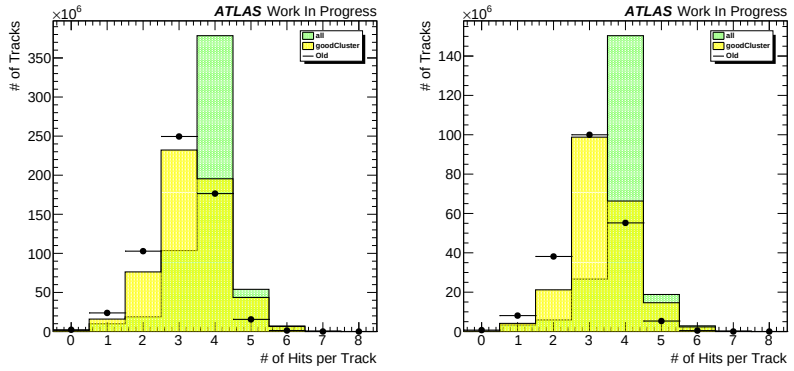

(a) Data (b) Monte Carlo

Figure 3.10: The Figure shows four examples of the fitting done to locate the most probable value of the charge for a given value of cos(α). These examples are from the first barrel layer, the fits where made separately for each layer.

The effect on the average number of hits per track shown in Figure 3.10 are written in numbers in Table 3.2 and shows slightly more hits per track by my cuts, which should result in a better precision of the dE/dx measurement.

Number of hits per track		
	Mean	Std
Data		
All	3.82	0.76
Old	3.10	0.90
New	3.34	0.96
MC		
All	3.89	0.72
Old	3.05	0.87
New	3.35	0.89

Table 3.2: The table shows the different cuts effect on the average number of hits per track.

3.3 Pixel dE/dx

Measuring the specific energy loss dE/dx of a track is done by measuring the dE/dx of each cluster generated by the track throughout the detector. It is derived from the cluster charge taking into account the average energy needed to create an electron-hole pair, W$= 3.68 \pm 0.2$eV/pair [1], the path in silicon and the density of silicon;

$$\frac{dE}{dx} = \frac{Q}{W}\frac{cos(\alpha)\rho}{d} \tag{3.1}$$

Where Q is the charge measured, ρ is the density of silicon, d is the thickness of the detector and α is the angle to the normal of the surface of the detector calculated by;

$$\alpha = \arctan\sqrt{\tan(\text{localPhi})^2 + \tan(\text{localTheta})^2} \tag{3.2}$$

Where both localPhi and localTheta are variables in the dataset.

As the Charge read-out in the detector is a factor in the calculation of dE/dx this measurement is dependent of the cuts made in the section above, histograms of the measurements of each cluster cut dependent is shown in Figure 3.11. The goal when trying to modify the dE/dx measurement is to get a peak as narrow as possible, the main result of my cuts is a higher peak around the MPV this is expected since as stated earlier my cuts allow more hits to be taken into account, than it is the case for the old cuts in [1]. A less expected gain from the new cluster selection cuts is the fact that the tail at low charge are effectively reduced, the source of this could very well be an effect of the cuts made in center region of the pixel modules since the charge read-out here, tended to be lower than the average as shown in Figure 3.5.

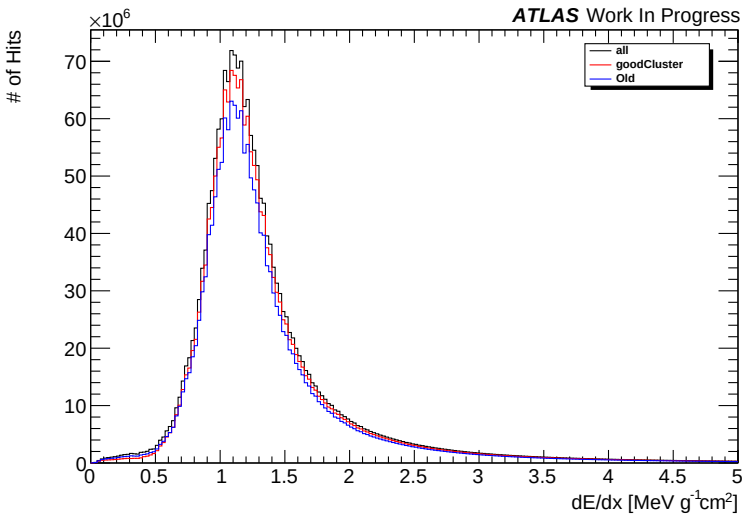

Figure 3.11: The histogram show the effect of the goodCluster cuts on the measurement dE/dx compared to the old cuts and if no cuts are made.

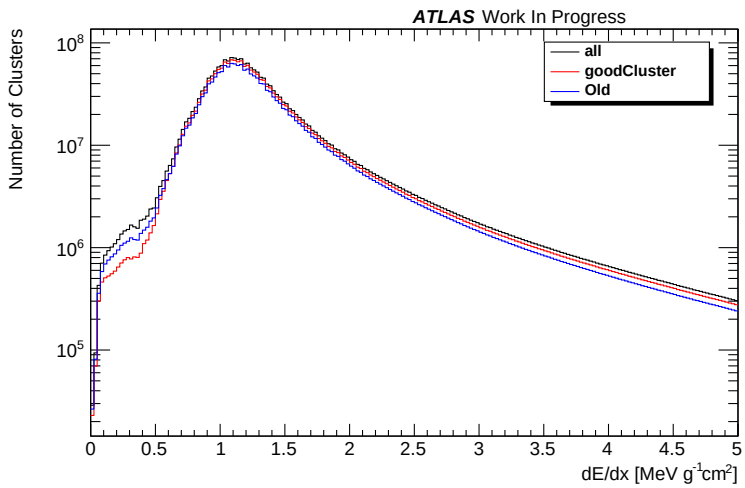

Figure 3.12: Same histogram as Figure 3.11 but with log scale on the y-axis to show the effect at low dE/dx.

3.3.1 Track dE/dx

The typical way of measuring dE/dx of a given track is to calculate the truncated mean of the dE/dx of the clusters associated with the track. This technique is frequently used when many ionization samplings are available [30] and the truncated mean is typically calculated averaging over the 70% lowest energy deposit measurements [1]. This is done to exclude measurements laying in the Landau tail and has the benefit of reducing the truncated mean to a Gaussian, providing an improved resolution of dE/dx. This technique is not possible to use in the case of the ATLAS Pixel Detector since only a few measurements per track are available as it was shown in Figure 3.10, therefore an alternative calculation is needed. The alternative way of measuring dE/dx is by excluding x amount of clusters with the highest dE/dx where x depends on the amount of clusters in the track, according to the prescriptions shown in Table 3.3.

Clusters excluded per track	
Clusters	Clusters Excluded
>=5	2
4	1
3	1
2	0
1	0

Table 3.3: The table shows the number of cluster excluded from the each track, depending on the number of measurements per track. The clusters removed are those with the highest dE/dx measurements.

This way of getting a measurement of dE/dx is necessary, since the restrictions on process-time of a given calculation make it hard to get a better measurement. One of the ideas in my thesis was to try another way of doing this dE/dx calculation, to see if it was possible to get a better measurement without adding too much extra process-time to the calculation for each track. The main idea was to find a function fitting the known distribution of dE/dx shown in Figure 3.11 and then use this to fit a maximum likelihood estimation eq. 3.3 to all measurements of the track, this way no measurements are excluded. The idea was that this would result in a narrowing of the peak from a smaller landau tail and thereby a shift of the average dE/dx to the left on the x-axis. The likelihood function:

$$L(\theta) = \prod_{i=1}^{n} f(x_i; \theta) \tag{3.3}$$

Where the likelihood function $L(\theta)$ is the probability density for the occurrence of a sample configuration $x_1, ..., x_n$ given that the probability density $f(x; \theta)$ with parameter θ is known.

Through fitting the dE/dx distribution measurements on tracks, I decided to use a function containing combination of a Gauss and a Landau distribution. I thought the only a Landau distribution was needed but it turned out to be too steep on the backside of the dE/dx distribution, therefore a Gauss was added to smoothen the drop. The result of the likelihood fitting can be seen on Fig. 3.13 compared to the result when the current method is used. Both histograms contains the same 5703 entries and is comparable. The fit-parameters of the two histograms are shown in Table 3.4, they show a narrowing of the peak when using the Likelihood approach and the MPV has moved closer to 1.00 which is the expected MPV value of the dE/dx distribution.

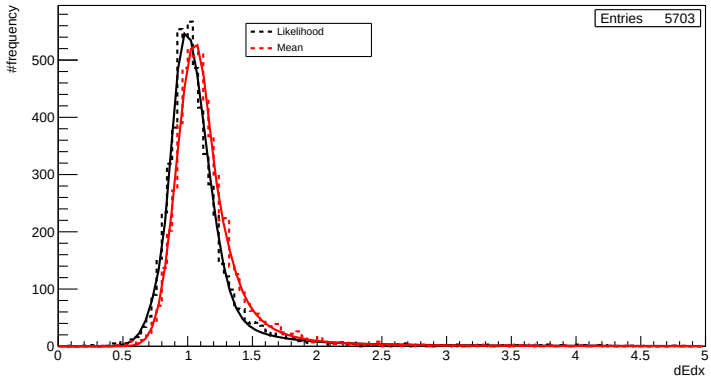

Figure 3.13: A comparing of two methods to calculate dE/dx for tracks in ID. The black dotted line is calculated by using a likelihood function, thereby using all measurement from the detector. The red dotted line is calculated by the current used method in ATLAS, where up to 2 point are excluded from the sample.

Fit parameters of Gauss Landau fits		
	Likelihood	Mean
c_1	3.52e2 $\pm$ 4.6e1	5.32e2 $\pm$ 1.02e1
μ_{gauss}	0.996 $\pm$ 0.006	1.055 $\pm$ 4.60e-3
σ_{gauss}	0.158 $\pm$ 4.60e-3	0.140 $\pm$ 3.23e-3
c_2	1.90e3 $\pm$ 1.43e2	4.87e2 $\pm$ 5.78e1
MPV_{landau}	1.00 $\pm$ 1.57e-2	1.34 $\pm$ 2.35e-2
σ_{landau}	0.078 $\pm$ 4.71e-3	0.082 $\pm$ 4.44e-3

Table 3.4: The Table contains the fit parameters of the two fit. The parameters show that the likelihood approach has a MPV closer to 1.0 and the width of the peak is smaller, than it is the case when using the Mean approach.

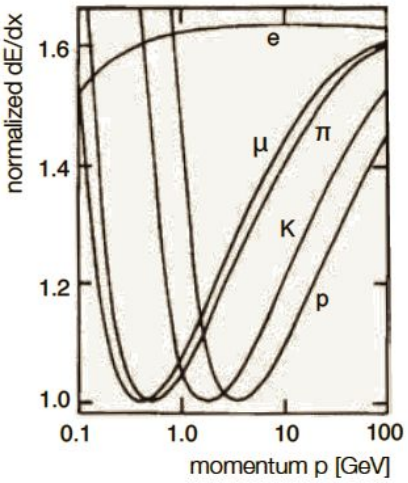

Figure 3.14: The graph shows the relativistic rise of dE/dx use for particle identification. I shows separation between Pions, Kaons and Protons making it possible to distinct these particles at low momentum. This can be interpreted as a zoom on Figure 1.3 [31].

The fitting of the two histograms show that when using the likelihood approach for calculating dE/dx of a given track, the distribution is closer to what would be expected. I would suggest this as a better approach than the one currently used, but through my analysis of this problem, I realized that the calculations when using the likelihood approach is more than 1000 times as demanding as the current approach calculating the mean by the rules shown in Table 3.3. As an example the test containing 5703 sample tracks I made before doing the calculation full scale took about 14 days. I tried to optimize the calculations by predefining the parameters of the fit but this only showed small improvements and the method never got to a point where it would be able to compete with the current method. I tried to run a full scale calculation of the track dE/dx measurement of my dataset, but I closed this job after one month of running since this runtime never would be acceptable in any kind of analysis.

3.4 The dependency of dE/dx on β

My supervisor Troels Petersen introduced me to a graph, showing the dE/dx dependency on β and asked me to try and remake this plot with my data. The plot can be seen on Figure 3.15 fitted with a three parameter function that is a simplification of the Bethe-Bloch formula 1.1.

$$dE/dx = \frac{C_0}{(\beta)^{C_2}} + C_1 \tag{3.4}$$

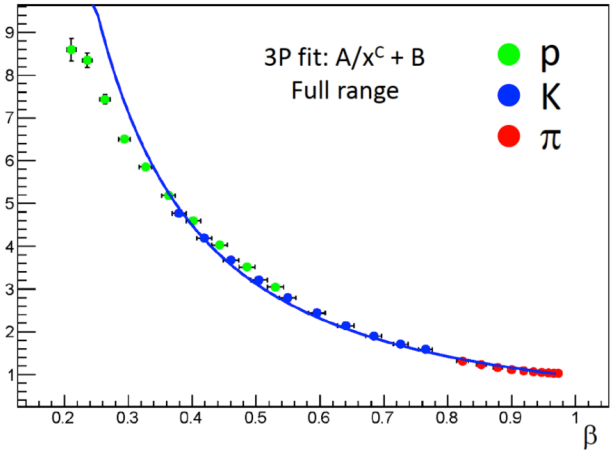

Figure 3.15: The plot shows the dependency of β on dE/dx, the plot is fitted with a simplification of the Bethe-Bloch equation.

3.4.1 Particle Identification

To do this I needed to be able to identify the different particles, since β is given by:

$$\beta = \sqrt{\frac{p^2}{m^2 \cdot p^2}} \tag{3.5}$$

where p is the momentum and m is the mass of the given particle, since the mass vary from different particles it is necessary to be able to identify these particles. This is done at low momentum where the relativistic rise shown in Figure 3.14 make it possible to separate the particles.

In my case I decided to focus on tracks with four Goodcluster hit throughout the detector. The reasons for this was that tracks with less hits have a larger uncertainty on the dE/dx measurement and most of the tracks with hits above six, will be tracked with double hits in some of the layers and thereby they traveled through more material than tracks with lower numbers of hits. The momentum compared to energy loss for particles with four hits is shown on Figure 3.16, the same plot for different numbers of Goodcluster hits can be seen in Appendices A.4.

Figure 3.16 clearly shows a separation between particles, matching the hypothesis that the sample contains three charged particle species respectively from lowest momentum peak and out: π, κ and Protons. Fitting these three peaks separately is done by subdividing the sample in a set of 40 dE/dx slices with logarithmically increasing width to take the decreasing amount of measurements as dE/dx increase into account. In earlier analysis [1] this has been done by slicing in momentum instead of dE/dx. I tested both approaches and found that by slicing in dE/dx the width of the peaks narrows which makes it easier to distinguish them, furthermore when slicing in the momentum axis you have to define when a peak is consumed by the big electron peak, this is also avoided by slicing in dE/dx as shown on Figure 3.17.

I used a function i ROOT called $TSpectrum()$ to search for peaks

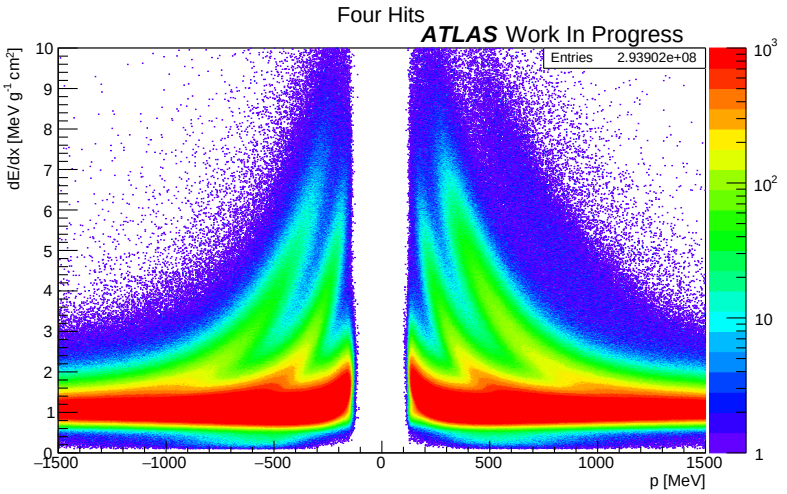

Figure 3.16: The plot show tracks dE/dx as a function of their momentum, the different particles are clearly separated at low momentum.

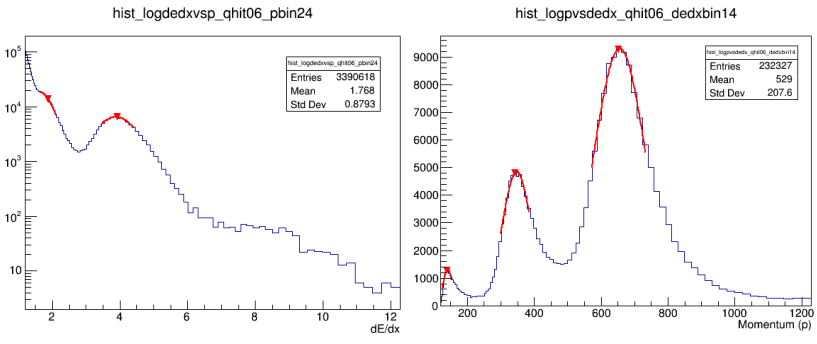

(a) Sliced in momentum

(b) Sliced in dE/dx

Figure 3.17: The two histograms shows the difference between slicing in momentum or dE/dx. When sliced in momentum as earlier analysis have done, the peaks are wider and the as a particle peak gets close to the electron peak, it gets harder to define whether or not it is still a peak belonging to the specific particle.

in the 2d histograms that was the result of the slicing, then I used the peak positions from the spectrum to fit Gaussian distributions to each top and thereby get the mean value of each peak. I got the momentum size and error from the mean μ and width σ of these fits and linked these values to the particle associated with the given peak. The dE/dx value was defined at the mean value of the given bin, the is can only be done when assuming that the dE/dx values of the point inside the bin is a even distribution, this is not the case as the amount of points increase as we move towards lower values of dE/dx. In our case we used 40 bins from $1.2 - 12.0\text{MeVg}^{-1}\text{cm}^2$ which is a high amount of bins in such a small interval, this will lead to a small error since the shift in dE/dx from skewing will be neglectable.

3.4.2 Fitting with my data

To get from the my current data consisting of dE/dx values for given momentum value, divided into particles. I need to convert the momentum into a value of β using equation 3.5, furthermore I use error propagation to find the error on β.

$$\sigma_\beta = \frac{d}{dp}\left(\sqrt{\frac{p^2}{m^2+p^2}}\right)\cdot\sigma_p \tag{3.6}$$

$$\sigma_\beta = \frac{m^2}{(m^2+p^2)^{3/2}}\cdot\sigma_p \tag{3.7}$$

Where m is the mass of the particle that made the track, p is the momentum in this case the μ_{peak} and σ_p is σ_{peak}. When I then plot the dependency of dE/dx on β as it was done on Figure 3.15, I get the graph shown in Figure 3.18. This plot is for the positive half of the particles, the same plot could have been made including both the positive particles and their negative counterparts but since I had plenty of data, I saw no reason to risk smearing the data. As the plot and fit shows the dependency seems to fulfill the simplification of the Bethe-Bloch equation, never the less at low β values there seems to be a mismatch between the fit and the actual observed dE/dx. This lead me into checking the momentum measurement, to see if any corrections were needed.

3.4.3 Momentum Correction

To test the momentum measurement the correct result has to be known, therefore the Monte Carlo sample is used since MC contains a truth container with the actual values that can be linked to all tracks in the detector. By comparing the measured value at the so-called truth value a ratio that describes how precise a measurement is can be obtained. Simply by dividing the reconstructed tracks momentum with the expected momentum linked in the truth container:

$$\text{Ratio} = p_{\text{reco}}/p_{\text{truth}} \tag{3.8}$$

This Ratio should be equal to 1, if the measured momentum is what it is supposed to be. The plots of this ratio for Kaons and Protons

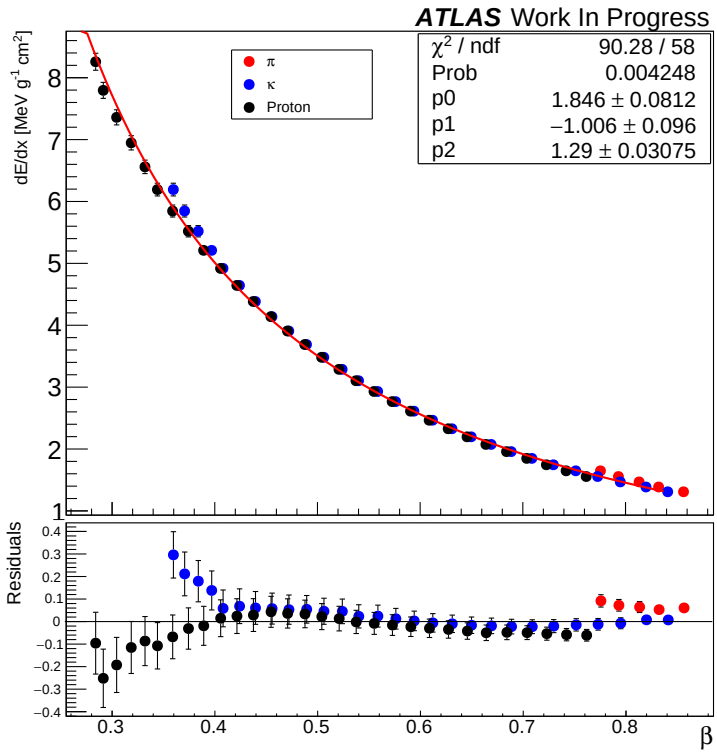

Figure 3.18: The plot show tracks dE/dx as a function of their momentum, the different particles are clearly separated at low momentum.

is shown respectively on Figure 3.19 and 3.20. It is clear that below 700MeV a shift happens between the measured value of the momentum and the truth value.

To correct for this misalignment I used the same $TProfile$ function as I used to define the cuts on the detector modules in Section 3.1, this profile returns the 3d histogram shown in Figure 3.20 as a 2d graph with momentum on the x-axis and the average of the ratio on the y-axis. To get a function of the correction needed at a given momentum I fit this Profile plot with the function:

$$f(x) = p_0 - p_1 * e^{-p_2 * \frac{x}{10^3} - p_3 * \frac{x^2}{10^6}} \tag{3.9}$$

The result of fitting this function to the Profile plot of Kaons and Proton is shown on Figure 3.21 and 3.22. The fit and the fitting parameters are used to correct the momentum measurement on the Kaons and Protons, the result should be a better fitting function than it is the case on Figure 3.18.

The dE/dx dependency on β plot after the momentum corrections are shown on Figure 3.23, it is clear that the momentum correction did not work as intended. The Kaons and Protons are supposed to follow the same dependency as it is the case on Figure 3.18, but after my correction this is not the case anymore. Furthermore even when fitting the particles' dE/dx to β dependence separately, especially the protons seem to fit the Bethe-Bloch simplification even worse (The lower fit stat box on Figure 3.23, the Kaon Fit is the upper fit box), mind the difference on the y-axis on the residual plot.

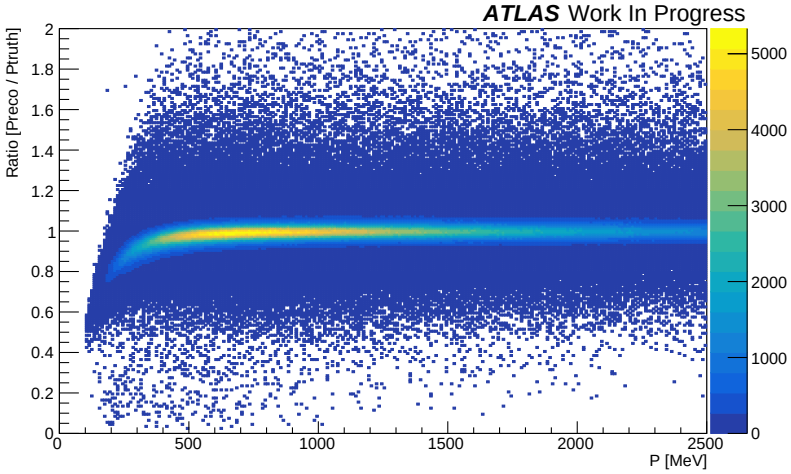

Figure 3.19: The graph shows the $p_{\text{reco}}/p_{\text{truth}}$ ratio for Kaons at a given momentum, the plot is used to test if a correction on the momentum measurement is needed.

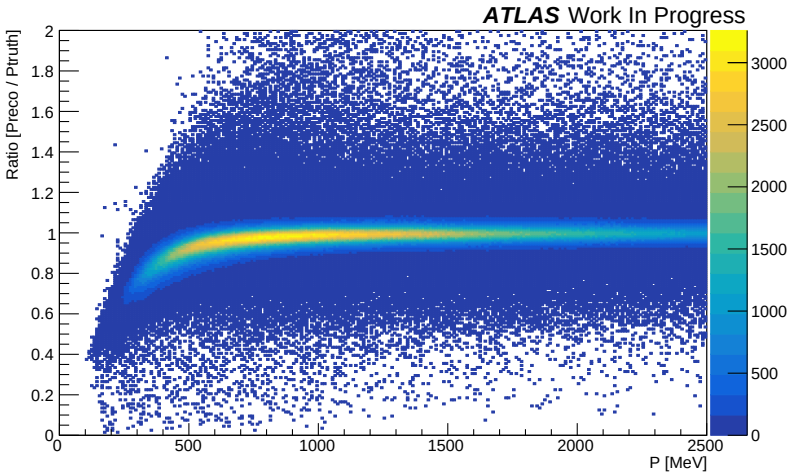

Figure 3.20: The graph shows the $p_{\text{reco}}/p_{\text{truth}}$ ratio for Protons at a given momentum, the plot is used to test if a correction on the momentum measurement is needed.

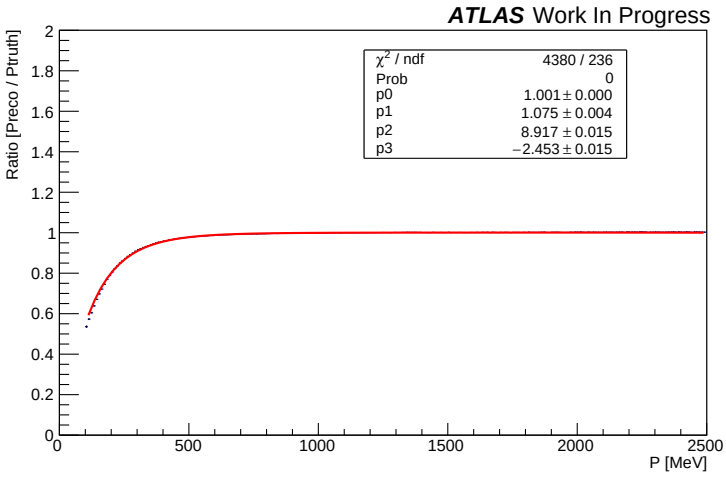

Figure 3.21: The plot shows the TProfile of Figure 3.19 fitted with eq. 3.9. The fit is used to correct the momentum measurement of the Kaon tracks.

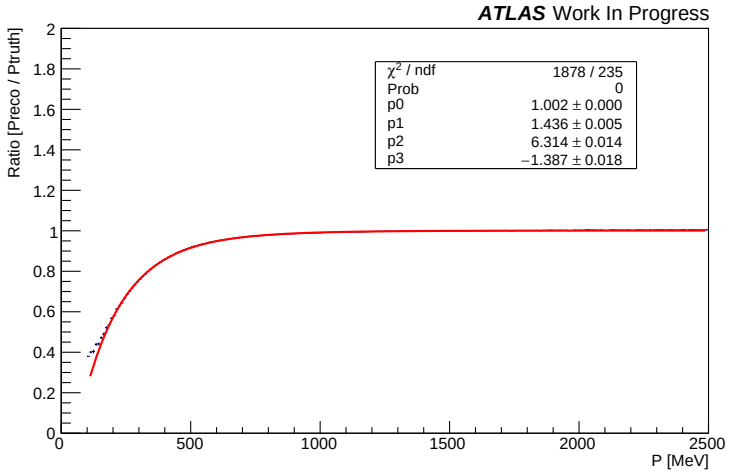

Figure 3.22: The plot shows the TProfile of Figure 3.20 fitted with eq. 3.9. The fit is used to correct the momentum measurement of the Proton tracks.

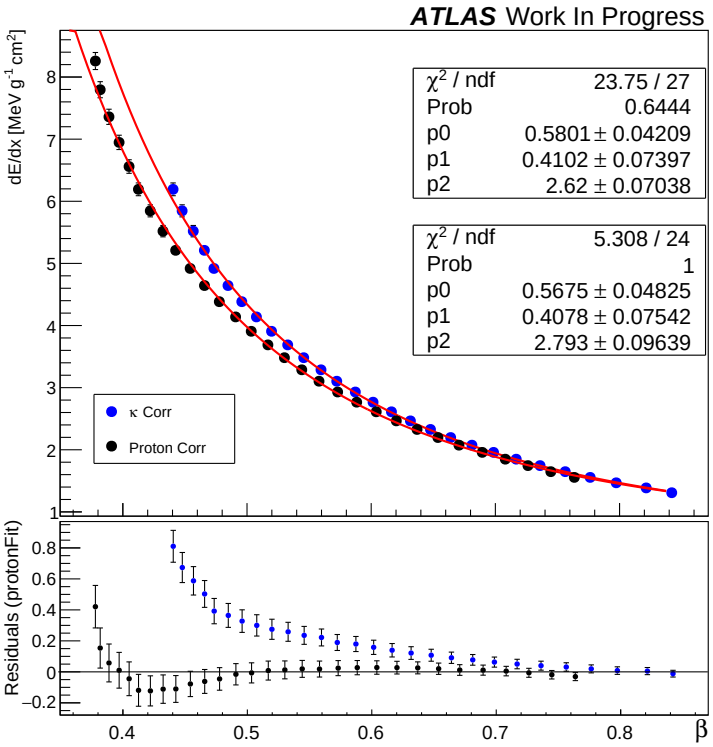

Figure 3.23: The plot shows dE/dx's dependency on β after the momentum correction. Both particles are fitted with eq. 3.4, the upper stat box is for Kaons and the lower Protons.

3.4.4 β uncertainty

As a addition to the study of the dE/dx dependency of β, Troels Petersen mentioned that the uncertainty on β had not be defined by anyone. People tended to use 13% as a standard but an experimental value would be useful now that I had all the data to do so.

I chose to use the dependency I found before my momentum corrections, since my corrected momentum dependency plot was less successful. By using eq. 3.4 to the fit on Figure 3.18 I get the

dependency between dE/dx and β, which rewritten is:

$$\beta = \left(-\frac{C_1 - dE/dx}{C_0} \right)^{1/C_2} \tag{3.10}$$

Resulting in an uncertainty equal to:

$$\sigma_\beta^2 = \left(\frac{\partial \beta}{\partial \frac{dE}{dx}} \right)^2 \sigma_{dE/dx}^2 \tag{3.11}$$

where

$$\frac{\partial \beta}{\partial \frac{dE}{dx}} = \frac{\left(\frac{dE/dx - C_1}{C_0} \right)^{1/C_2}}{C_2 (C_1 - dE/dx)} \tag{3.12}$$

When inserting the parameters from the fit on Figure 3.18 into eq. 3.11, $\sigma\beta$ as a function of dE/dx is shown on Figure 3.24. The plot show that the uncertainty on β is not constant, and that the uncertainty is dependent on the size of dE/dx. For this study I used the histograms that are sliced in momentum, as it is shown on Figure 3.17 $\sigma dE/dx$ increases as dE/dx decrease, this is a result of the particles peak being consumed by the m.i.p. peak, therefore I would estimate that the $\sigma\beta$ found is only useful above 2.5 on the x-axis. Above this limit this sample is really small, but the uncertainty on β seems to increase as dE/dx increases.

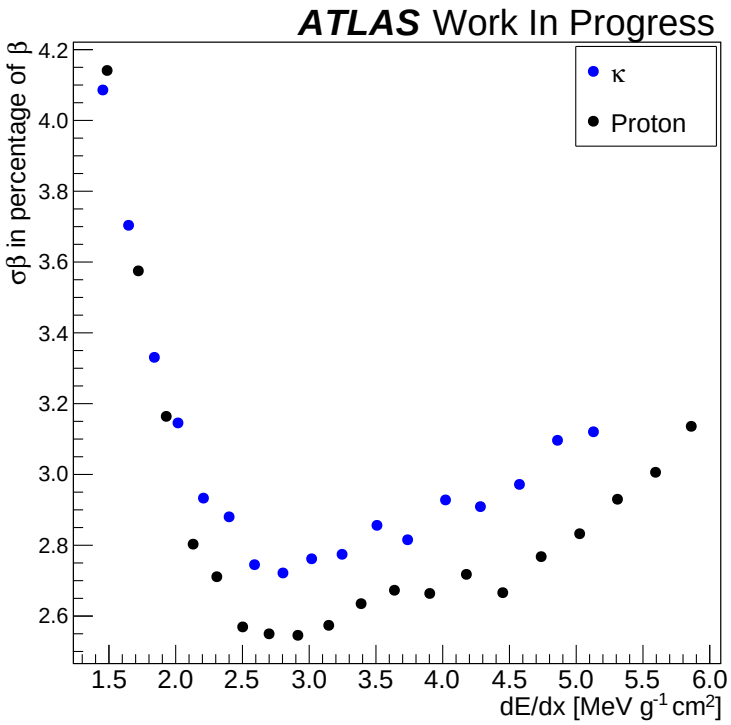

Figure 3.24: The plot shows the $\sigma\beta$ in percentage of β as a function of dE/dx, it is clear the $\sigma\beta$ in this case is a dependent on dE/dx.

To overcome this challenge of the increase in $\sigma dE/dx$, I tried to preform the same study with the histograms sliced in dE/dx. But since the size of the bins are logarithmically increasing a dE/dx

increase, this result in a misleading logarithmic relation shown on Figure 3.25.

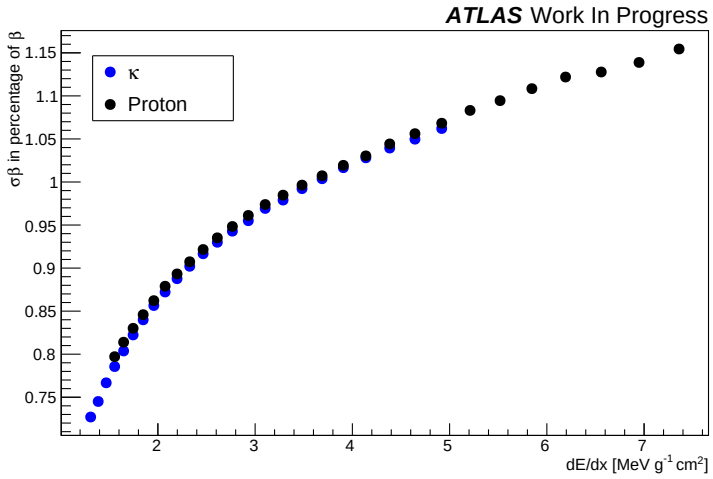

Figure 3.25: The plot shows the $\sigma\beta$ in percentage of β as a function of dE/dx, when using the histograms produces by slicing in dE/dx.

3.5 Concluding remarks

3.5.1 Summary

This thesis has presented a study of the dE/dx measurement in the ATLAS detector.

The Good Cluster study made an attempt on defining new cuts when determining which clusters should be used as Good Clusters. It was well known that the ID modules charge read-out is mis-leading close to the edge of the module, but the study also showed abnormalities close to the center of the modules. In earlier studies a cut in $\cos(\alpha)$ was made since clusters with $\cos(\alpha)$ below 0.16 had a misalignment with the simulations and was therefore removed. This study was not able to locate any misalignments, and the cut might be unnecessary.

The dE/dx study attempted to improve the uncertainty of a track's dE/dx, by fitting a likelihood function the tracks dE/dx measurements. This procedure turned out to claim much more process-time than the currently used method, even though the small test showned promising results the solution would not in its current form have any use, due to the unacceptable process requirements.

The study of the dependency of dE/dx on β compare the data of this study with a similar study, and show a good agreement with this study. In the search of optimizing the dependency fit to a simplified Bethe-Bloch formula, the measured momentum was compared to the truth momentum, this showed a correction need at low dE/dx. But when the needed correction measured using MC was applied to real data, this correction shifted the dependency of dE/dx on β resulting in a split between different particles. The reason behind the difference in MC and Data is unclear to me, but as a result of this split between different particles the momentum correction was not applied to the remaining part of this study. The last part of this study attempted to define a uncertainty of β, the result implies that this uncertainty is dE/dx dependent.

3.5.2 Outlook

This study only touch the surface of a topic that does not seem that well studied, the last official article was published back in 2011, before the last upgrade of the ATLAS detector.

The study of how a Good Cluster is defined reveals parts of the ID modules, that seems to provide misleading measurements of the charge. A future study might try to divide these modules into smaller segments, to look for differences in this charge read-out in each layer.

The attempt to decrease the uncertainty on the dE/dx measurement was discarded early in the process, due to unacceptable processing requirements. A new study might try a different approach to this objective, since the current method does not take the distribution of the dE/dx measurement into account, when calculating the mean. An approach which in some degree includes the knowl-

edge of the distribution, should improve the accuracy of the dE/dx measurement.

The study of the uncertainty on β showned an uncertainty depending on dE/dx, but the dependency was smeared by the measurement of $\sigma dE/dx$. A solution to this could be to run a study on a MC sample, and simply only allow kaons and protons, this way the m.i.p. peak would desperate and $\sigma dE/dx$ would be measurable at low values of dE/dx. This should make it possible to get a relation between $\sigma\beta$ and dE/dx.

Appendices

A.1 Datasets

Table A.1: The data samples provided for this analysis, these data samples differs from most samples since they cover low momentum measurements down to 100 MeV.

Type	DSID	Name
Data	299315	calibration_PixelBeam.recon.DAOD_IDTRKVALID.r8077
MC	361203	Pythia8_A2_MSTW2008LO_ND_minbias.recon.DAOD_IDTRKVALID.e3639_s2601_s2132_r8383

A.2 Pixel Detector Coverage

The histograms below show the η coverage of the Pixel Detector.

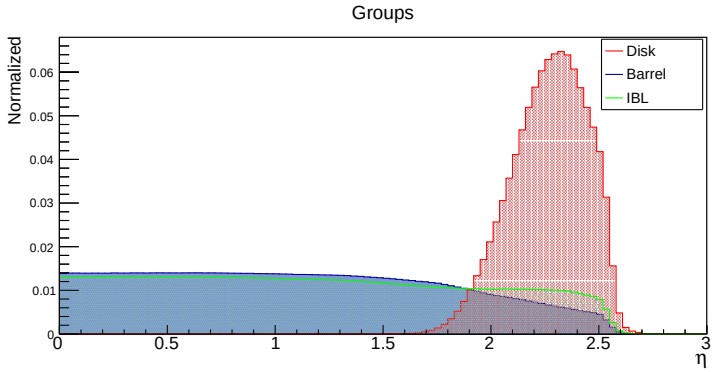

Figure A.1: The figure shows how the different parts of the Pixel Detector covers the η.

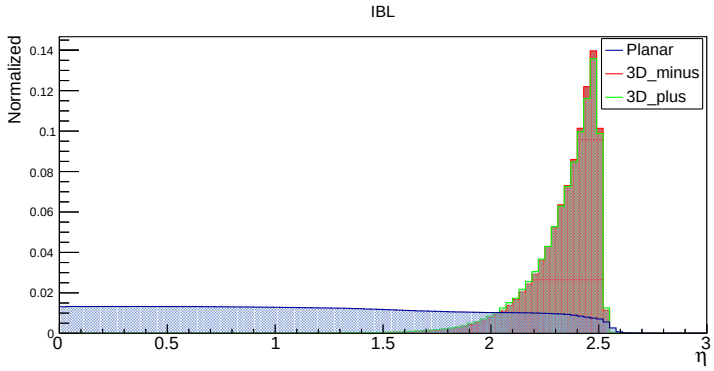

Figure A.2: The figure shows how the three different parts of the IBL covers the η.

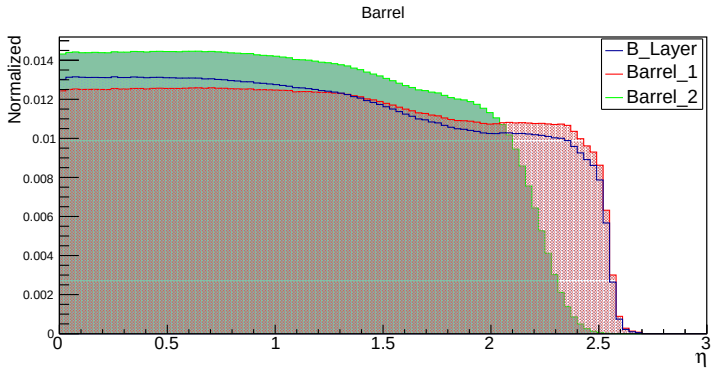

Figure A.3: The figure shows how the different Barrels covers the η..

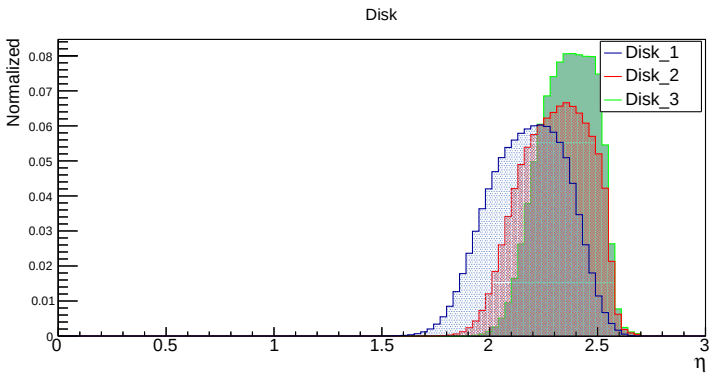

Figure A.4: The figure shows how the different three disks of the Pixel Detector covers the η..

A.3 Good Cluster

A.3.1 IBL and End Cap

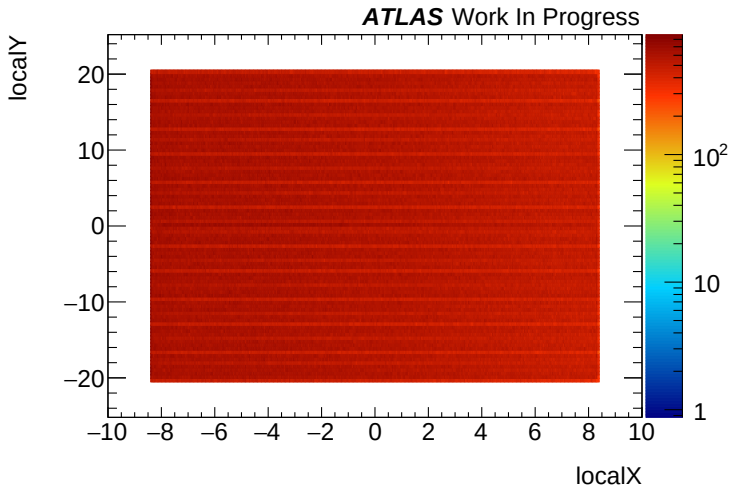

Figure A.5: The plot shows the distribution of the cluster locations on the IBL pixel modules. The distribution can be considered even since the checkered pattern originate from ROOTs drawing and alters when you change the since of the figure.

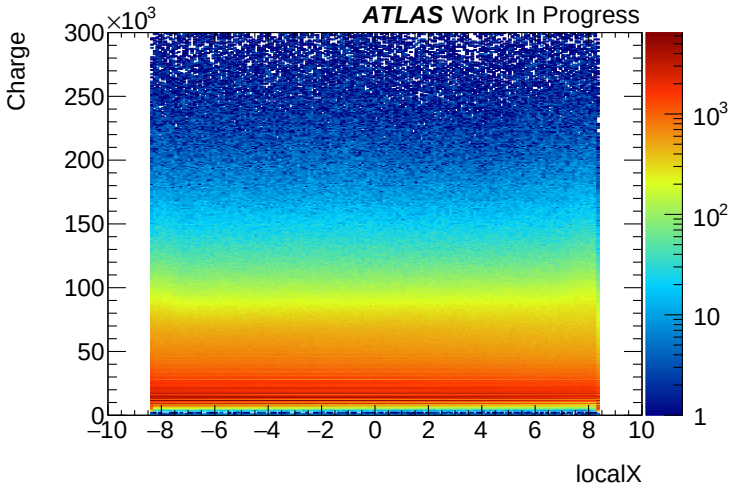

Figure A.6: IBL: This plot visualize the distribution of the charge measurements for a given location on the x-axis, this is used to locate areas that returns unreliable information.

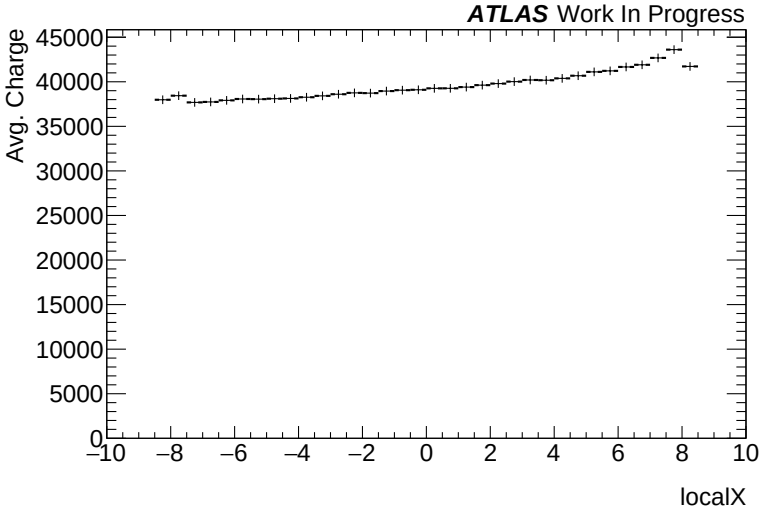

Figure A.7: IBL: The Profile plot of localX is used to define cuts.

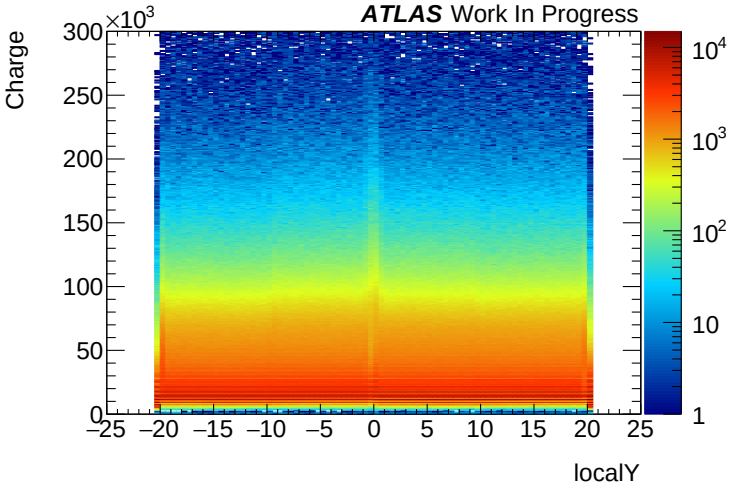

Figure A.8: IBL: This plot visualize the distribution of the charge measurements for a given location on the y-axis, this is used to locate areas that returns unreliable information.

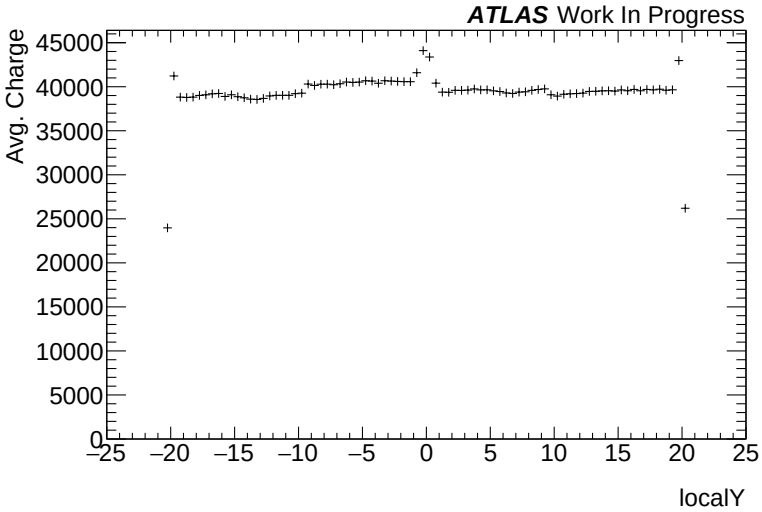

Figure A.9: IBL: The Profile plot of localY is used to define cuts.

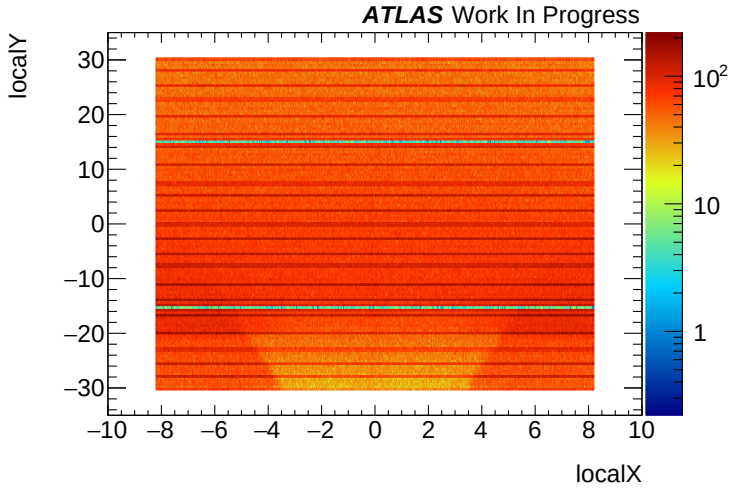

Figure A.10: End Cap: The plot shows the distribution of the cluster locations on the End Cap pixel modules. Although it is not at big effect it is clear that the close the module is to the beam line the more clusters will hit the module, this gradient of hit is also visible on the LocalY Profil in Figure A.14. Furthermore the fact that the modules are square and have to overlap to form a disk, is also visible is the lower part of the plot.

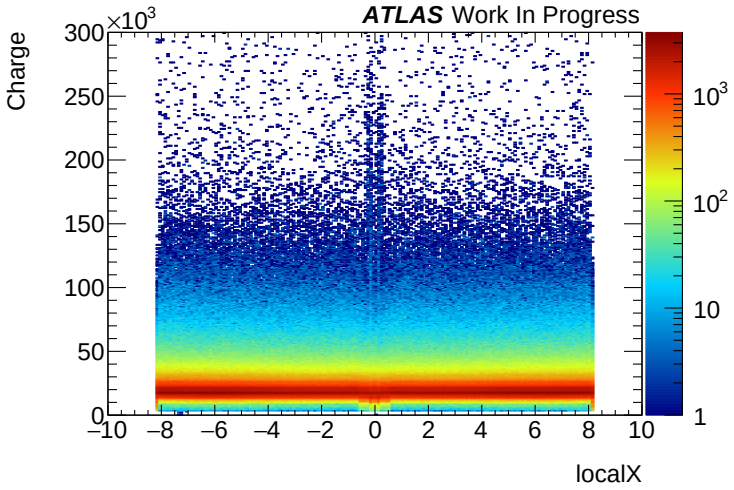

Figure A.11: End Cap: This plot visualize the distribution of the charge measurements for a given location on the x-axis, this is used to locate areas that returns unreliable information.

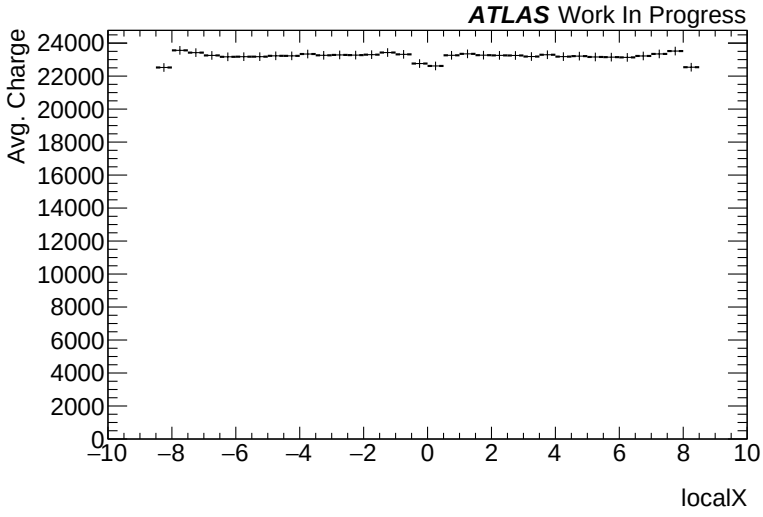

Figure A.12: End Cap: The Profile plot of localX is used to define cuts..

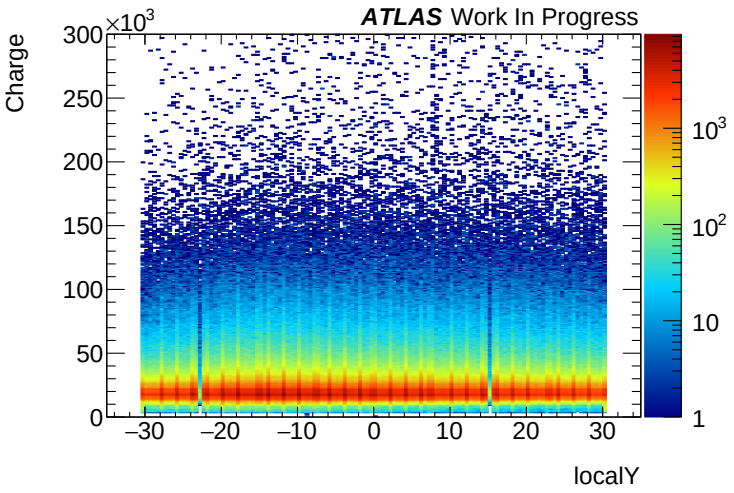

Figure A.13: End Cap: This plot visualize the distribution of the charge measurements for a given location on the y-axis, this is used to locate areas that returns unreliable information.

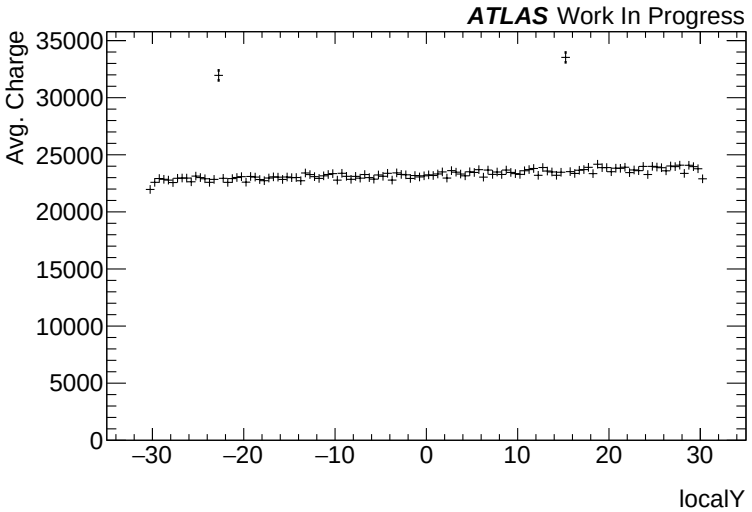

Figure A.14: End Cap: The Profile plot of localY is used to define cuts.

A.4 dE/dx as a function of momentum p

The plots below show the dE/dx as a function of momentum, for different amounts of Good Cluster hits.

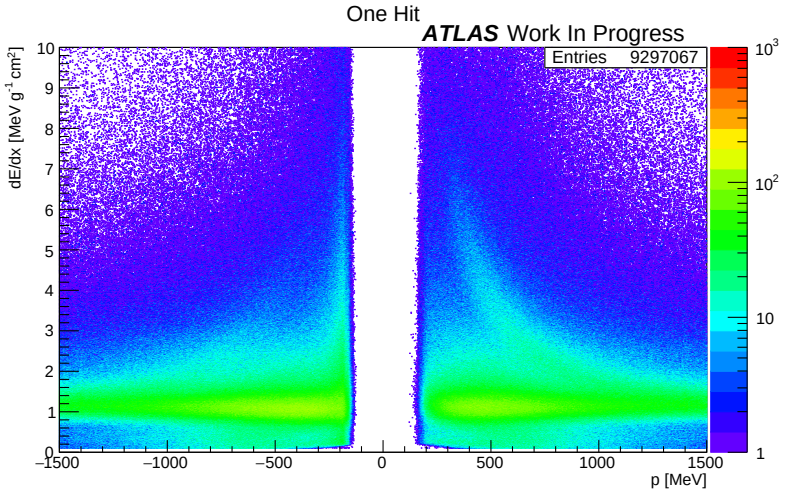

Figure A.15: One Good Cluster hit.

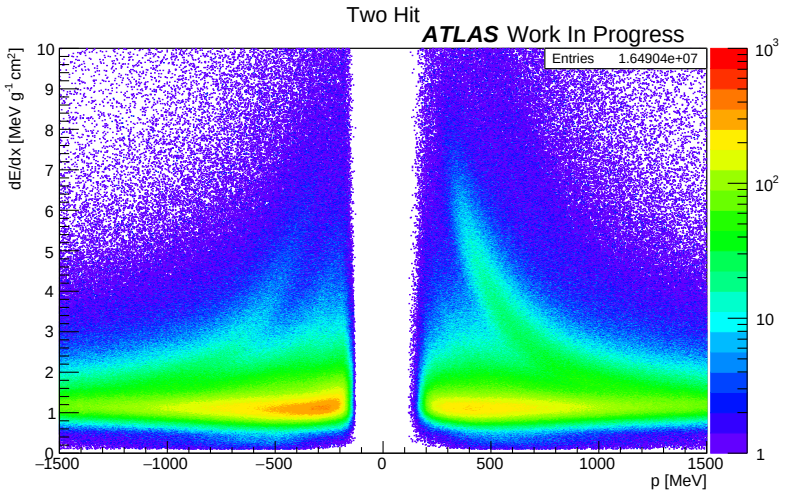

Figure A.16: Two Good Cluster hits.

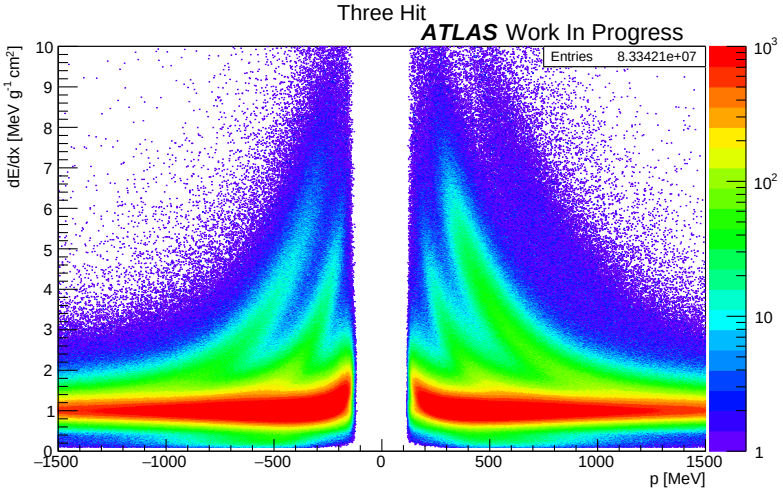

Figure A.17: Three Good Cluster hits.

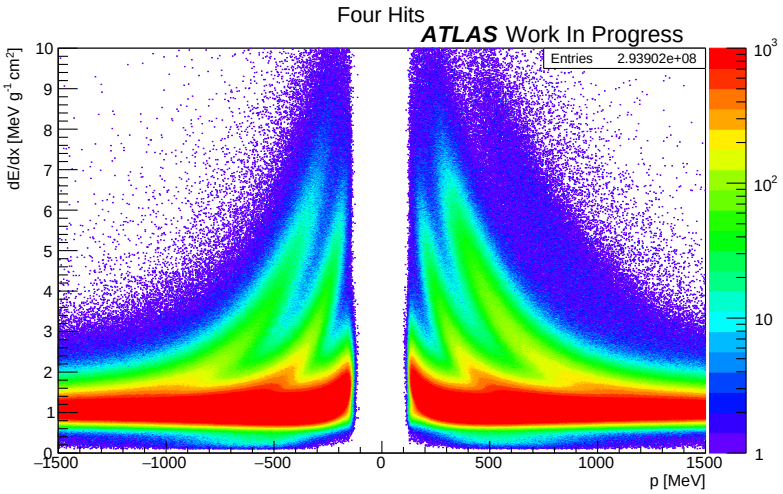

Figure A.18: Four Good Cluster hits.

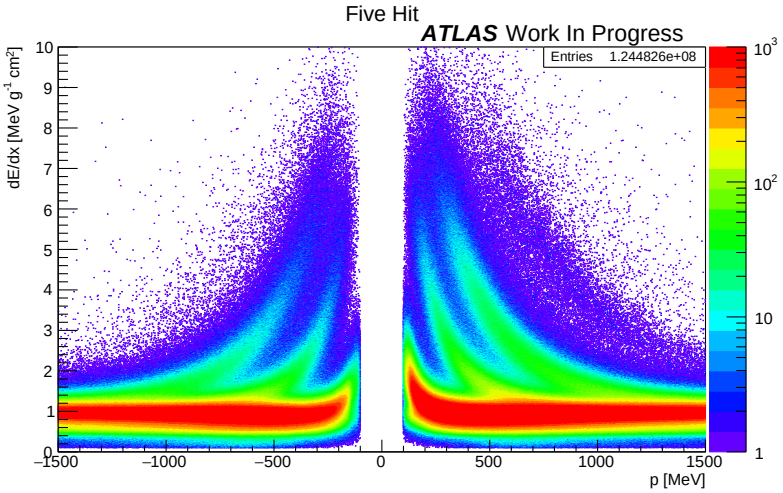

Figure A.19: Five Good Cluster hits.

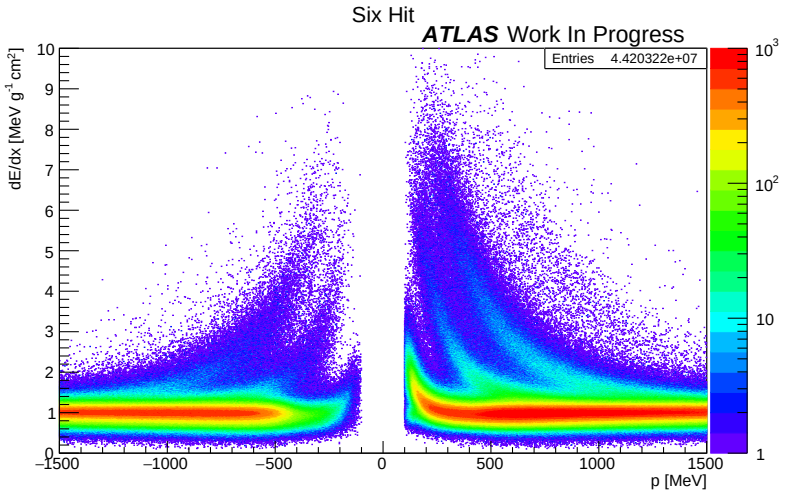

Figure A.20: Above six Good Cluster hits.

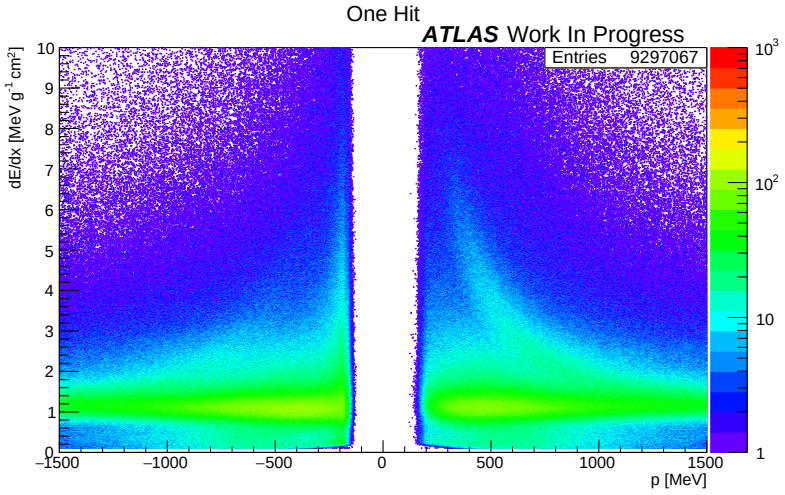

Figure A.21: The figure shows how the different parts of the Pixel Detector covers the η.

References

[1] The ATLAS Collaboration. dE=dx measurement in the ATLAS Pixel Detector and its use for particle identification. *ATLAS NOTE*, (ATL-ATLAS-CONF-2011-016), 2011.

[2] Wikipedia. Standdart Model, 2016. [Online; accessed 22-December-2016].

[3] ATLAS Collaboration (G. Aad *et al.*). The ATLAS Experiment at the CERN Large Hadron Collider. *JINST*, **3**(S08003), 2008. [inSPIRE:796888].

[4] Jlorn Grosse-Knetter. Vertex Measurement at a Hadron Collider - The ATLAS Pixel Detector. *BOON-IR-2008-04*, **1**(ISSN-0172-8741), 2008.

[5] H. Bethe. Bremsformal fÃijr Elektron relativisticher Geschwindigkeit. *Z. Phys. 76*, (293), 1932.

[6] C. Amsler, Revised by H. Bichsel, D.E. Groom and S.R. Klein. Passage of Particles Through Matter. *pdg*, **1**(B667), 2010. [inSPIRE:PL B667].

[7] J.D. Jackson. Classical Electrodynamics. *John Wiley and Sons, Inc.*, (New York), 1975.

[8] L. Landau. On the enrgy loss of fast particles by ionization. *J.Phys.(USSR) 8*, (201), 1944.

[9] H. Bichsel. Straggling in thin silicon detectors. *Rev. Mod. Phys. 60*, (663), 1988.

[10] Y.S. Tsai. Pair Production and bremsstrahlung of charged leptons. *Rev. Mod. Phys. 46*, (815), 1974.

[11] S. Meroli, D. Passeri and L. Servoli. Energy loss measurement for charged particles in very thin silicon layers. *JINST*, **6**(P06013), 2011.

[12] Robert N. Cherry, Jr. Encyclopaedia of Occupational Health and Safety, 2016. [http://www.ilocis.org/documents/chpt48e.htm].

[13] G.R. Lynch and O.I. Dahl. Approximations to multiple Coulomb scattering. *Nuclear Instr. Meth. B 58*, (6), 1991.

[14] European Organization for nuclear research. LHC DESIGN REPORT: Vol. 1 The LHC Main Ring. Technical Report CERN-2004-003, CERN, Geneva, June 2004.

[15] Guillaume Unal and Luca Fiorini. Integrated luminosity summary plots for 2011-2012 data taking, 2011. [Online; accessed 31-August-2016].

[16] Eric Torrence. Luminosity summary plots for 2015 pp data taking, 2015. [Online; accessed 31-August-2016].

[17] Eric Torrence. Luminosity summary plots for 2016 pp data taking, 2015. [Online; accessed 31-August-2016].

[18] T. Ihn. *Semiconductor Nanostructures*. Oxford University Press, 4th edition, 2013. ISBN 978-0-19-953442-5.

[19] W. Leo. Techniques for nuclear and particle physics experiments: a how to approach. *Springer*, 1994.

[20] M. Krammer and F. Hartmann. Silicon Detectors. Lecture slides, 2011.

[21] Julia Rieger. Detector Development for the High Luminosity Large Hadron Collider. Technical Report CERN-2016-090, CERN, Geneva, 8 2016.

[22] C. Kittel. *Introduction to Solid State Physics*. John Wiley and Sons, Inc, 8th edition, 2005. ISBN 978-0-471-41526-8.

[23] http://www.pcmag.com/encyclopedia/term/47578/n-type-silicon.

[24] P.P. Altermatt. Reassessment of the intrinsic carrier density in crystalline silicon in view of band-gap narrowing. *J. Appl- Phys. 93*, 3(1598), 2003.

[25] Peter Hansen. Particle detectors and accelerators. Lecture Notes, 2015.

[26] https://twiki.cern.ch/twiki/pub/AtlasPublic/TRTPublicResults/RTrelation_run264034_barrel_4.pdf.

[27] https://twiki.cern.ch/twiki/bin/view/AtlasPublic/PixelPublicResults.

[28] https://twiki.cern.ch/twiki/pub/AtlasPublic/L1MuonTriggerPublicResults/fig_09.pdf.

[29] J. Beringer et al. Review of Particle Properties. *Phys.Rev. D86*, (010001), 2012.

[30] W. Blum and G. Rolandi. Particle Detection with Drift Chambers. *Springler-Verlag*, (Berlin Heidelberg), 2013.

[31] Garutti. Lecture Note 12, 2017. [http://www.desy.de/~garutti/LECTURES/ParticleDetectorSS12/L12_PID.pdf].

dE/dx MEASUREMENTS IN THE ATLAS DETECTOR